LA-SUB--95-74

" Study of Chip-Breaking Mechanisms in Orthogonal Cutting "

Covering the Period April 1, 1990 - June 30, 1991

Technical Report

University of California
Los Alamos National Laboratory
Subcontract 9-XM0-F7372-1

Submitted by

John S. Strenkowski
Principal Investigator
North Carolina State University
Raleigh, NC

July 15, 1991

Acknowledgement

The following students participated in the preparation of this report as part of their research for their graduate degrees :

Shounak Athavale

Juhchin Yang

Table of Contents

1	**Introduction**		1
2	**Review of the Orthogonal Cutting Model (Task 1)**		2
	2.1	Formulation of the visco-plastic model	2
	2.2	Temperature calculation	6
	2.3	Calculation of the total plastic strain	7
	2.4	Determination of the chip geometry	9
	2.5	Simulating frictional behavior	12
3	**Theoretical Formulation of a Chip Breaking Model (Task 2)**		14
4	**Application of the Chip Breaking Models (Tasks 3 and 4)**		21
	4.1	Experimental cutting tests : techniques and apparatus	21
	4.2	Cutting forces	24
	4.3	Chip geometry	30
	4.4	Chip temperatures	42
	4.5	Chip breaking tests and model results	44
5	**Summary and Conclusions**		55
	5.1	Future Work	56
6	**References**		57

1. Introduction

This report summarizes the activities of the research project entitled "Study of Chip Breaking Mechanisms in Orthogonal Cutting". The research effort took place from April 1990 to June 1991.

The overall objective of the project was to develop a systematic procedure for gaining a more fundamental understanding of chip breaking mechanics. Central to this objective is a computer model that can simulate chip formation in orthogonal cutting. This model has been under development for the past seven years at NCSU. The model is based on an Eulerian formulation of the finite element technique. The model simulates the cutting process for various tool geometries over a wide range of cutting conditions. The model can be used to predict chip geometry, cutting forces, plastic strains, strain rates, and temperatures in the workpiece and chip, as well as temperatures in the tool itself. Of particular significance is that specific tool geometries can be simulated. Therefore, the model can be used to systematically evaluate the strains, strain rates, temperature, and geometry of the chip as a function of a specific chip-breaker tool design. These results can provide the crucial information necessary to formulate a fundamental understanding of the chip breaking mechanism over a wide range of operating conditions and workpiece materials.

In this project, the cutting model was modified to allow for the simulation of groove-type chip breaker tools. With this modification, the model can be used to predict the chip geometry for prescribed cutting conditions and chip breaker tool geometries. Once the chip geometry has been determined, the continued chip deformation can be evaluated. For this stage of the deformation, a model of the chip was developed using an updated Lagrangian code called NIKE2D. Good correlation was found between the computed stresses and the resulting chips in the experiments.

The chip breaking model was verified with orthogonal cutting tests on 1020 steel. Experiments were performed for a range of cutting speeds from 40 to 120 inch/second for depths of cut from 0.0032 to 0.0091 inch. Both flat and chip breaker inserts were tested and excellent correlation was found between the measured tool forces, chip thickness, and chip forms and results from the computer cutting model simulations.

The following sections of this report describe the results of this research project for the various tasks. In Section 2, the theoretical formulation of the cutting model is reviewed in terms of its applicability for modeling groove-type chip breaker tools (Task 1). A model of chip breaking is discussed in Section 3 (Task 2). In Section 4, the models are applied to specific cases and compared with the chip breaking experiments (Tasks 3 and 4). Section 5 summarizes the conclusions from this research project and also describes future work.

2. Review of the Orthogonal Cutting Model (Task 1)

The orthogonal cutting process can be modeled with an Eulerian formulation of the finite element technique. In this formulation, the finite element grid defines a control volume through which the workpiece and chip flow. An advantage of this approach is that the over-distortions that sometimes occur with a Lagrangian model are avoided. Another is that steady-state conditions can be modeled directly. This eliminates the lengthy transition from incipient cutting conditions and the need for an explicit parting line criterion required by a Lagrangian model. A disadvantage of this approach is that the chip geometry is more difficult to calculate because the grid is not attached to the workpiece. Therefore, a so-called free surface algorithm must be used to determine the chip geometry, which is found by iteratively adjusting the free surfaces of the chip until the velocity vectors on the surfaces have a zero normal component.

The following subsections describe various aspects of the model which are essential for accurately simulating chip formation.

2.1 Formulation of the visco-plastic material model

In metal machining, the plastic deformations are so large that the elastic deformation (strain) can be neglected. In this case, the material flow can be treated as a viscous, incompressible, Non-Newtonian flow. From the Navier-Stokes equation, the constitutive equation of stress and strain rate for steady state, viscous, incompressible flow is given by:

$$S_{ij} = \sigma_{ij} - \delta_{ij}\sigma_m = 2\,\mu\,\dot{\varepsilon}_{ij} \qquad (2.1)$$

S_{ij} : the deviatoric stress
σ_m : the mean stress
σ_{ij} : the stress components
δ_{ij} : the kroneker delta (if i=j, δ_{ij}=1; otherwise δ_{ij}= 0)
$\dot{\varepsilon}_{ij}$: the strain rate component
μ : the viscosity which can be a function of strain rate

The governing equation of viscoplastic flow can be derived through the introduction of the yield criteria into the above equation. Adopting the viscoplastic model as suggested by Perzyna [1] and later used by Zienkiewicz [2], the material behavior is described by the following equation:

$$\dot{\varepsilon}_{ij} = \frac{1}{\mu}\,\langle F \rangle \frac{\partial Q}{\partial \sigma_{ij}} \qquad (2.2)$$

where $\bar{\mu}$ is the coefficient of viscosity and the F is the yield surface where F = F(s) = 0 represents the plastic yielding condition. The notation $\langle\ \rangle$ is interpreted as:

$\langle F \rangle = 0$ if $F<0$ (no flow)

$\langle F \rangle = F$ if $F>0$ (flow starts).

The parameter Q is defined as the plastic potential which is identical to F for associated flow. Using the von Mises's yield criteria, then F is defined as :

$$F = \sqrt{3\,J2} - \sigma_y \qquad (2.3)$$

where σ_y is the uniaxial yield stress and J2 is the second invariant of the deviatoric stress. By substituting Eq.(2.1) and Eq.(2.3) into Eq.(2.2), the general governing equation for viscoplastic flow can be found to be given by:

$$\mu = \frac{\sigma_y}{\sqrt{3}\,\dot{\varepsilon}} + \bar{\mu} \qquad (2.4)$$

Note that for ideal plasticity for which there is no work hardening, $\bar{\mu} = 0$ and this equation can be rewritten as:

$$\mu = \frac{\sigma_y}{\sqrt{3}\,\dot{\varepsilon}} \qquad (2.5)$$

where the yield stress can be a function of temperature and strain rate. Because the viscosity becomes infinite at zero strain rate, a cut-off value for viscosity is necessary in order to prevent numerical problems.

Using the above equations, the constitutive equations can be written in the following matrix form:

$$\{\sigma\} = [D]\{\dot{\varepsilon}\} \qquad (2.6)$$

where

$$[D] = \mu \begin{bmatrix} 2 & 0 & 0 \\ 0 & 2 & 0 \\ 0 & 0 & 2 \end{bmatrix} + (k - \frac{2\mu}{3}) \begin{bmatrix} 1 & 1 & 0 \\ 1 & 1 & 0 \\ 0 & 0 & 0 \end{bmatrix}$$

Boundary conditions for the velocity must be prescribed to complete the description of the problem. The velocity at the left boundary of the workpiece is assumed to be the cutting speed as shown in Fig. 2.1. On the lower boundary of the workpiece, the velocity is assumed to flow in the cutting direction. For the chip, there are three free surfaces. Because the land length of the grooved tool is generally smaller than the natural contact length, the land length of the grooved tool can be defined as the final contact length. Simulating of a groove-type insert requires first modeling a restricted contact tool. If the chip flows in the direction shown as the dotted line in Fig. 2.1, then it is assumed that the chip will contact the upper corner of the groove at point **E** and the simulation is then run with the chip in contact at this point. Note that a frictional condition is assumed wherever the chip contacts the tool. Therefore, two points must be used to represent the chip/tool contact at point **E** as shown in the inset in Fig. 2.1.

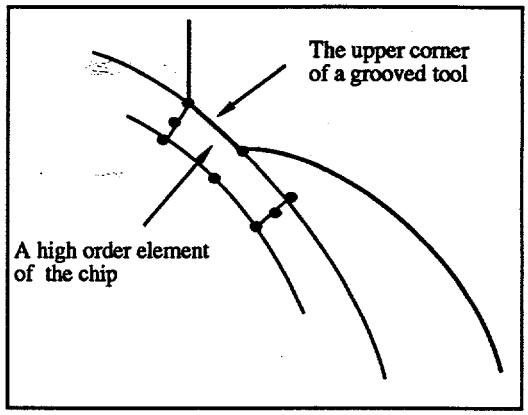

Enlarged view near point E

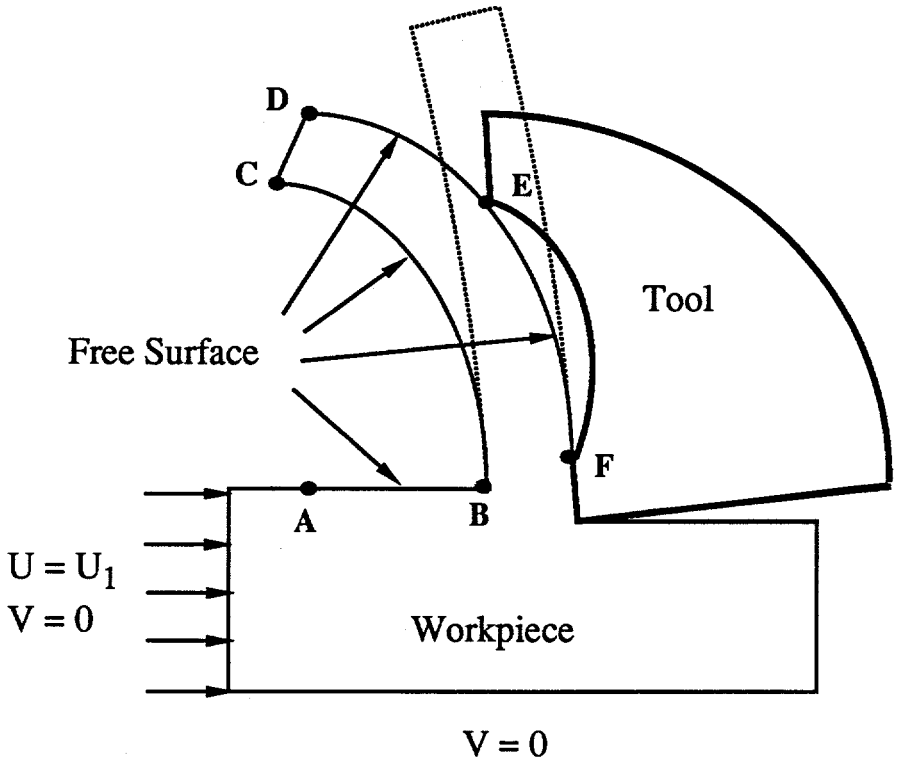

Fig. 2.1 Boundary conditions for velocity

2.2 Temperature calculation

Heat is generated by two sources in metal cutting. One is due to plastic work and the other is due to the frictional behavior between the chip and tool rake face. Heat due to plastic work can be calculated directly from the effective stress and strain rate, and frictional heating can be determined if the friction coefficient and the contact length are known.

The workpiece, chip, and tool can be treated as a two dimensional, steady state, heat conduction / convection problem. Based on a balance of energy, the temperature is governed by the following partial differential equation :

$$K\frac{\partial T}{\partial x^2} + K\frac{\partial T}{\partial y^2} - \rho\, C_p \left(u\frac{\partial T}{\partial x} + v\frac{\partial T}{\partial y} \right) + \dot{Q} = 0 \qquad (2.7)$$

where K is the thermal conductivity, r is the density, C_p is the specific heat, and $\dot{Q}$ is the rate of heat generation per unit volume. It is assumed that there is no heat loss in the entire system. The heat contributed from plastic work is defined as :

$$\dot{Q}_p = \frac{1}{V}\int \bar{\sigma}\,\bar{\varepsilon_p}\; dV \qquad (2.8)$$

where $\bar{\sigma}$ is the effective stress, $\bar{\varepsilon_p}$ is the effective strain rate, and V is the volume of elements.

The heat due to friction is defined by:

$$\dot{Q}_f = \tau_f\; V_f \qquad (2.9)$$

where t_f is the shear stress on the contact length, and V_f is the sliding velocity along the rake face. A Galerkin approach of the finite element method can be used to calculate the temperature in the workpiece and the tool.

To complete the description of the temperature problem, boundary conditions must be prescribed. Temperatures at the inlet and lower boundaries of the workpiece are prescribed, while the other surfaces of the chip and workpiece are assumed to be insulated as shown in Fig. 2.2. Because only a small portion of the tool is included in the cutting model, the tool boundary in the model is really an interior boundary, on which the temperature is unknown. A more accurate way to treat this interior boundary is to use a so-called infinite element [3] along the tool boundary. In an infinite element, one of the element edges is simply extended to

infinity by using appropriate shape functions. The infinite element has been successfully applied to a wide range of unbounded field problems.

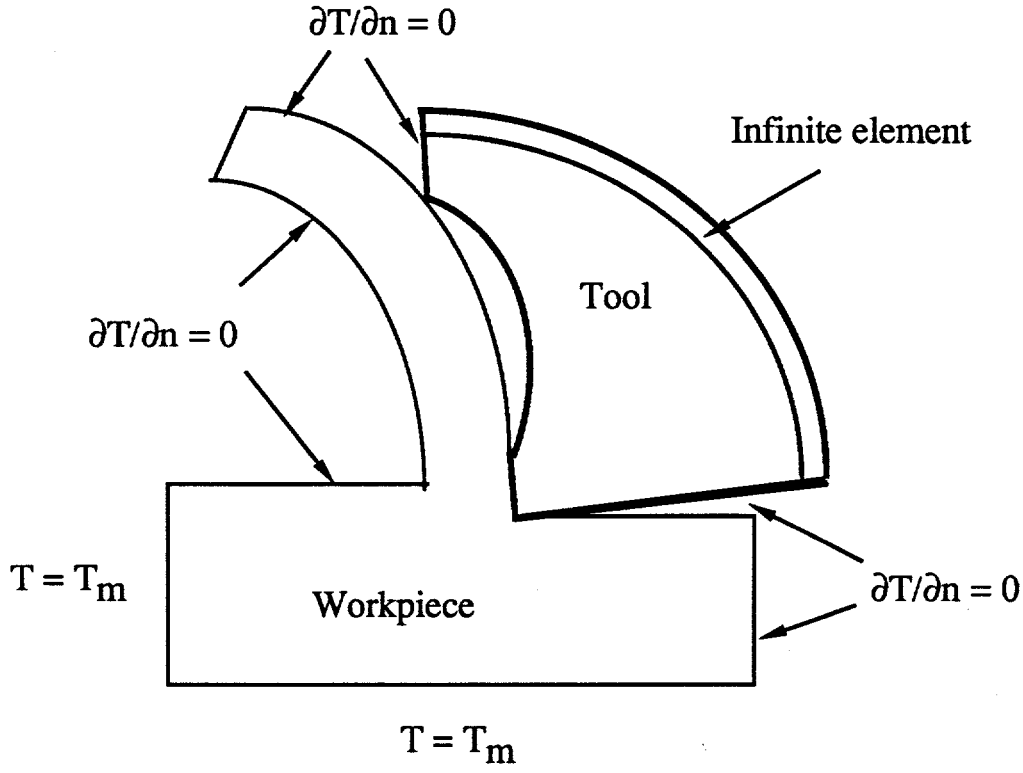

Fig. 2.2 Thermal boundary conditions

2.3 Calculation of the total plastic strain

Strain is an important factor in determining whether a chip will fracture. Because the cutting model has been formulated in an Eulerian frame, strain cannot be predicted directly. Therefore, an integration technique must be applied to determine the total strain in the workpiece.

The strain within an Eulerian reference frame can be determined by integrating strain rate along the streamline as follows:

$$[\varepsilon] = \int_0^t [\dot{\varepsilon}]\, dt \qquad (2.10)$$

where $[\varepsilon]$ is the strain, $[\dot{\varepsilon}]$ is the strain rate, and t is the time. This integration is performed between two nodes along a streamline. The distance between these two nodes is given by :

$$ds = u_s\, dt \qquad (2.11)$$

where ds is a differential streamline segment and u_s is the nodal velocity along the streamline. Substituting Eq.(2.11) into Eq.(2.10), the integral equation becomes :

$$[\varepsilon] = \int_0^s \frac{[\dot{\varepsilon}]}{u_s}\, ds \qquad (2.12)$$

The strain rate and velocities are determined for each element. Therefore, the integral must be replaced with a summation in the cutting model. That is,

$$[\varepsilon] = \sum_{n=1}^{N} \frac{[\varepsilon]^n}{u_s^n} |ds| \qquad (2.13)$$

$$x^n = x^{n-1} - |ds| \qquad (2.14)$$

where ds is the incremental distance between adjacent nodes on a streamline.

In the cutting model the center point of each element is used as the starting point for the strain integration scheme. The incremental distance depends on the size of the specific element. When an incremental distance is made along the streamline, it is necessary to know the velocity and strain rate of that new position so that the incremental strain can be calculated. A conventional bilinear interpolation scheme is used in which the four nodes at the corners of the element in which the new position is located are used. All the strain components are calculated with this scheme. Although this integral scheme is computationally intensive, it provides a reliable technique for determining the total strain in an Eulerian reference frame.

2.4 Determination of the chip geometry

An important parameter for determining whether a chip will break is its geometry after initial chip formation. To determine the chip geometry, a Galerkin technique can be applied to each element in which the mass flux across the boundary is minimized. That is,

$$U_S \eta_S = 0 \qquad (2.15)$$

$$u_s = u_x \hat{i} + u_y \hat{j} \quad ; \quad \eta_s = \frac{dy}{ds}\hat{i} - \frac{dx}{ds}\hat{j}$$

where u_S is the velocity vector, and η_S is the unit normal vector. A weighted residual can be formed based on the above constraint to give:

$$w_s = \int_S (u_S \eta_s) N_s \, ds = 0 \qquad (2.16)$$

where Ns is the element shape functions. The current coordinates (x,y) and the new unknown coordinates (X,Y) can be related by :

$$x = [Ns]\{X\};$$

$$y = [Ns]\{Y\}$$

Substituting x, y into the above equations gives :

$$[K_1]\{X\} - [K_2]\{Y\} = 0 \qquad (2.17)$$

where,

$$[K_1] = \int u_y [N]^T [N]' \, ds \quad ; \quad [K_2] = \int u_x [N]^T [N]' \, ds \qquad (2.18)$$

From Eq. (2.18), $[K_1]$ and $[K_2]$ can be found if u_x ,u_y are known. Substituting $[K_1]$ and $[K_2]$ into Eq.(2.17), then {X} and {Y} can also be found. Note that there is only one equation Eq.(2.17), but two unknowns {X}, {Y}. Therefore, an extra constraint is necessary to solve this problem. The additional constraint to find {X} and {Y}is that the length of each element is fixed.

Using this procedure, the free surface can be modified based on the velocities computed in each iteration step. This process is continued until there is no change in the free surface geometry. As an example, Figs. 2.5 and 2.6 show the chip geometry before and after the free surface algorithm has been applied.

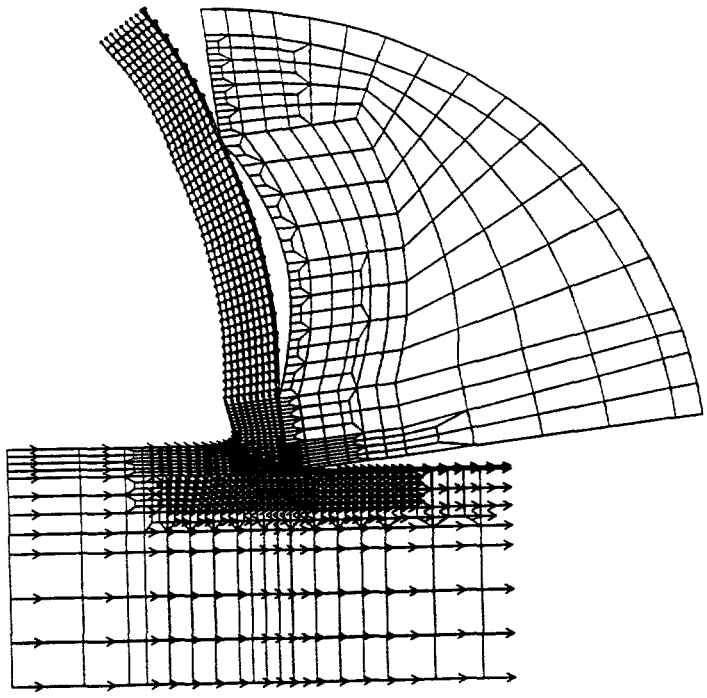

Fig. 2.5 Estimated chip geometry

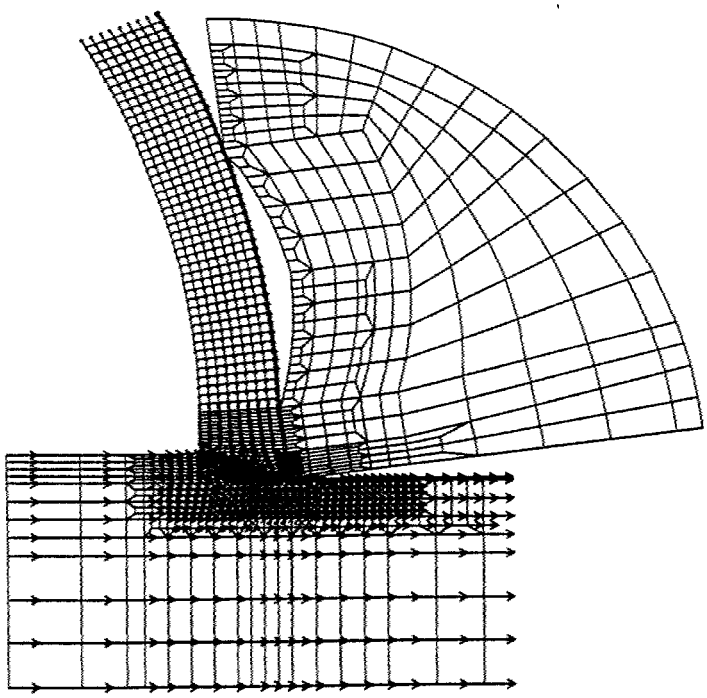

Fig. 2.6 Predicted chip geometry

2.5 Simulating frictional behavior

A so-called friction element introduced by Zienkiewicz [4] was used to simulate the friction behavior in the cutting model. This friction element has been used successfully in extrusion and other metal processing simulations. The basic idea of the friction element is that a narrow interface element is inserted between the rake face and the underside of chip. A constant friction coefficient is then applied to the side which is attached to the tool to simulate the friction behavior.

Although this element works well for simulating frictional behavior, it is also found that the stress distribution on the rake face suffers from the so-called "checkerboard syndrome". This is a numerical instability that causes stresses of large magnitude to change sign between adjacent elements. In the case of the cutting problem, the pressure along the rake face results in the sporadic oscillation shown in Fig. 2.7.

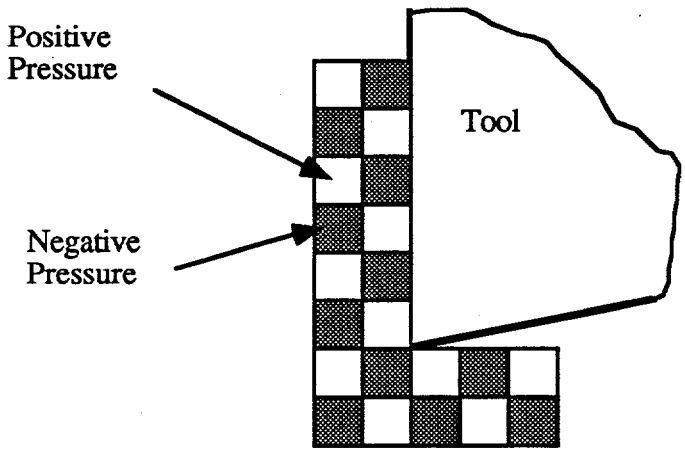

Fig. 2.7 The "checkerboard syndrome".

There are two ways to eliminate this problem. One is to use a higher order element. The other is to use a filtering scheme suggested by Sani [5]. In this scheme, a combination of the discretized continuity equations for each element which surrounds a single point is combined linearly as shown in Fig. 2.8. The general formula for this scheme is given by

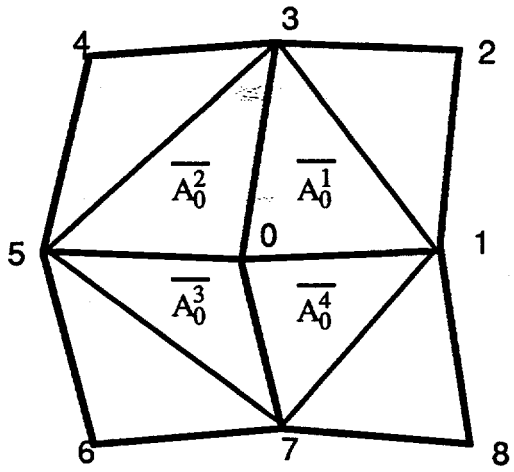

Fig. 2.8 Triangular areas used in the filtering scheme

$$p_0 = \frac{\sum_{i=1}^{4} p_i \overline{A_0^i}}{\sum_{i=1}^{4} \overline{A_0^i}} \qquad (2.19)$$

where P is the pressure, and A is the area of an element.

In the cutting model, a higher order element was used for the friction element, while the filtering scheme was applied to the other elements. As an example of the effectiveness of this scheme, Fig. 2.9 shows the pressure distribution along the rake face of the tool. As expected, the pressure decreases monotonically from the cutting edge of the tool.

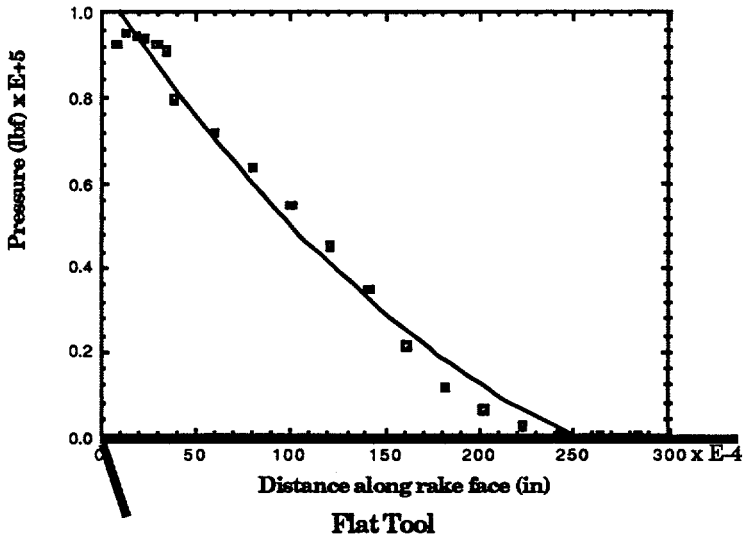

Fig. 2.9 Pressure distribution along contact face of the flat tool

3. Theoretical Formulation of a Chip Breaking Model (Task 2)

The cutting model described in the previous section simulates steady state chip formation during the cutting process. The shape and size of the resulting chip is determined by cutting conditions, workpiece material and thermal properties, and the tool geometry. The chip geometry may be characterized by its thickness and curvature. Once the chip has been formed, the chip flow will be determined by how it interacts with the tool geometry. Ultimately, the chip will continue to deform until the stresses in the chip exceed the strength of the material.

Chip breaker tools have been designed to modify the natural chip flow. Chip breaking occurs when the curled chip makes contact with either the tool itself, or the workpiece or flank face of the tool. There are two broad categories of chip breaker tools, as shown in Fig. 3.1. In an obstruction-type breaker, the chip flow is redirected by the tool. In a groove-type tool, the chip flows partially into the groove which alters the chip geometry. The objective of an obstruction-type breaker is to fracture the chip near the tool cutting edge. In contrast, a groove-type breaker deflects the chip in such a way so that it contacts either the workpiece or the tool flank face.

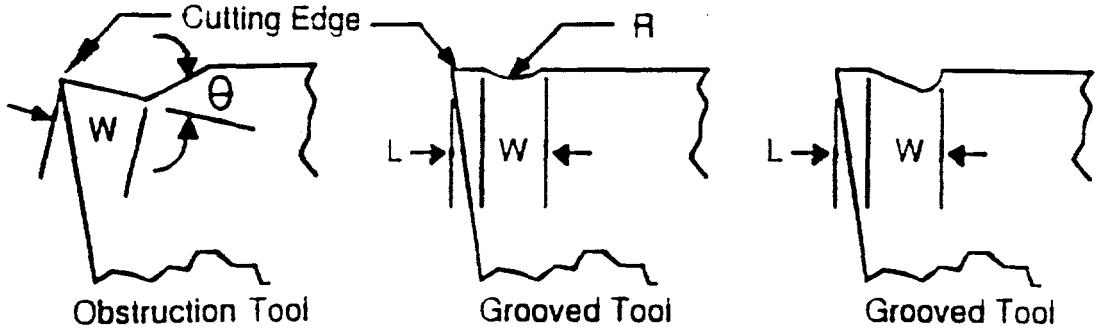

Figure 3.1 Chip breaker tool geometries

Figure 3.2 shows typical chip breaking with an obstruction-type tool. The chip breaker deflects the chip away from the tool, which reduces the radius of curvature. This type of breaker does not rely on the chip following a definite path after it has been formed, and as a result it represents a more reliable method for breaking chips.

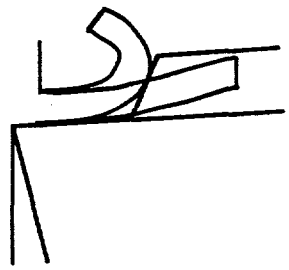

Figure 3.2 Chip breaking by obstruction-type tool

Figure 3.3 shows chip breaking with a groove-type tool. As the curled chip continues to form, it will contact the flank face of the tool. Note that it can also contact the workpiece. The chip cannot withstand any additional stress until the free end of the chip contacts the tool in some way. Once attached, the continued formation of the chip causes it to open up, thereby increasing the radius of curvature. The tensile stress increases until the material strength is exceeded and the chip fractures at point A.

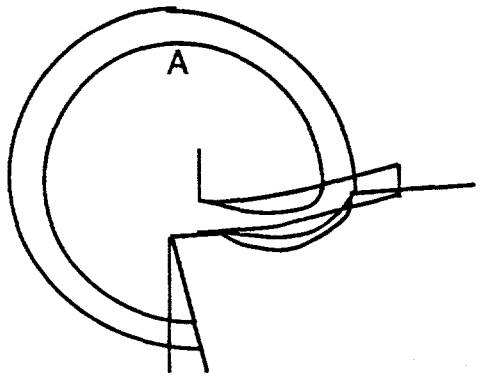

Figure 3.3 Chip breaking by groove-type tool

The primary advantage of an obstruction-type breaker is the predictable chip that it produces. However, it is not possible to design this type of tool that will consistently break chips over a wide range of feeds and speeds. Therefore, chip breaking due to hitting other parts of the tool and its support structure offer another means for breaking chips.

For the groove-type tools studied in this project it was found that the chips consistently fractured by contacting the flank face of the tool. Therefore, a plane strain model of this type of chip breaking was developed. In this model it is assumed that the chip becomes attached to the tool flank, and that it maintains its initial circular geometry. The dependence of the strain in the chip due to geometric changes can be determined by treating the chip as a curved beam. The strain ε in the chip is given by:

$$\varepsilon = \frac{h}{2}\left(\frac{1}{R_i} - \frac{1}{R_f}\right) = \frac{h}{2R_i}\left(1 - \frac{R_i}{R_f}\right) \tag{3.1}$$

where R_i and R_f are the initial and the final radii of the chip, and h is the chip thickness. The above equation can be rearranged into the following form:

$$\frac{\Delta R}{R_i} = \frac{1}{\left(\frac{h}{2\,\varepsilon\,R_i}\right) - 1} \tag{3.2}$$

where ΔR is the change in radius or difference in R_f and R_i. Also it can be shown that

$$\frac{\Delta R}{R_i} = \frac{\Delta C}{C_i} \tag{3.3}$$

where ΔC is the change in the circumference and C_i is the initial circumference. Therefore, the change in circumference ΔC required to reach the failure strain ε can be found from these equations.

Based on the previous theoretical analysis, a finite element model of the continued deformation of the chip can be developed. Figure 3.4 shows the geometry of the chip as predicted by the orthogonal cutting model for a Carbolloy TNMG 432-E-48 insert at a cutting speed of 40 in/sec and a depth of cut of 0.005 inch/rev. The chip extends from point A to point B. The circular support from C to D is intended to guide the chip along a circular path. The radius of curvature of this guide was determined from the initial chip geometry predicted by the orthogonal cutting model. The end of the guide at point D represents the point on the tool where the chip separates from the tool.

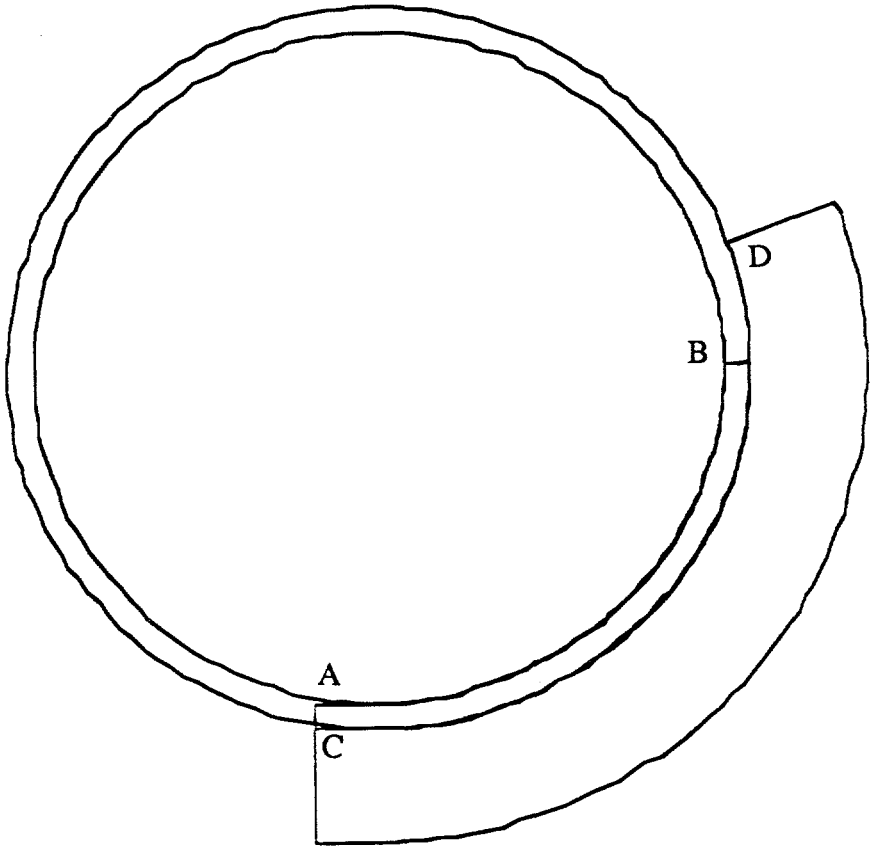

Figure 3.4 Initial geometry for the chip breaking model

The large deformation code NIKE2D was used to model the chip deformation. The contact between the chip and the circular guide was treated as a frictionless sliding contact in NIKE2D. Figure 3.5 shows the chip after a prescribed displacement of 0.04 inches has been applied to the chip at point A. This prescribed displacement was determined from equations (3.2) and (3.3) and a yield strain of 10^{-3} in/in, which corresponds to a yield stress of 30 X 10^3 psi. Note that the other end of the chip (B) was assumed to be pinned at its centerpoint. This boundary condition represents the frictional attachment of the chip to the flank face of the tool.

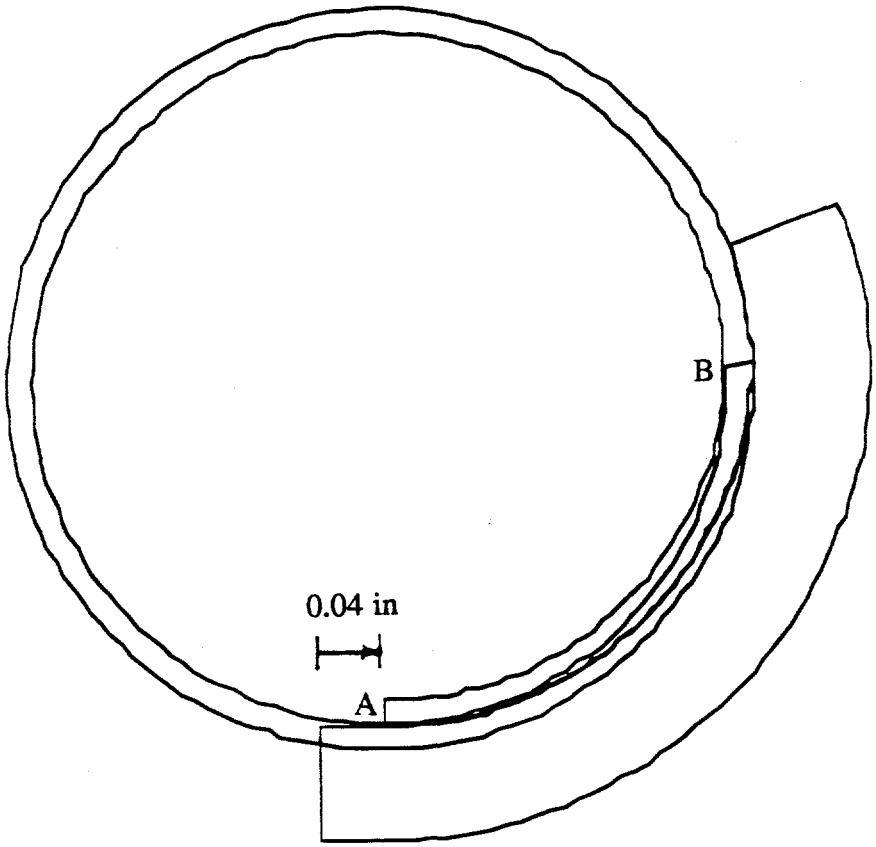

Figure 3.5 Final geometry for the chip breaking model

The stresses were computed throughout the chip. Figure 3.6 shows the maximum principal stress contours in the chip. The highest stress occurs at the inside of the chip at the point A in Fig. 3.6. This corresponds to a tensile longitudinal stress, which would cause the chip to fracture if the material strength were exceeded. This location of the chip fracture is consistent with past research and the experimental findings of this project, which will be discussed in Section 4 of this report.

The precondition for fracture of the chip at point A in Fig. 3.6 is that the free end of the chip remains in contact with the flank face of the tool. Stresses that are necessary to fracture the chip can only occur if the free end remains in contact. This requires that the chip be sufficiently stiff and

that the frictional force between the chip and the flank face is large enough to withstand out-of-plane forces that cause the chip to slip.

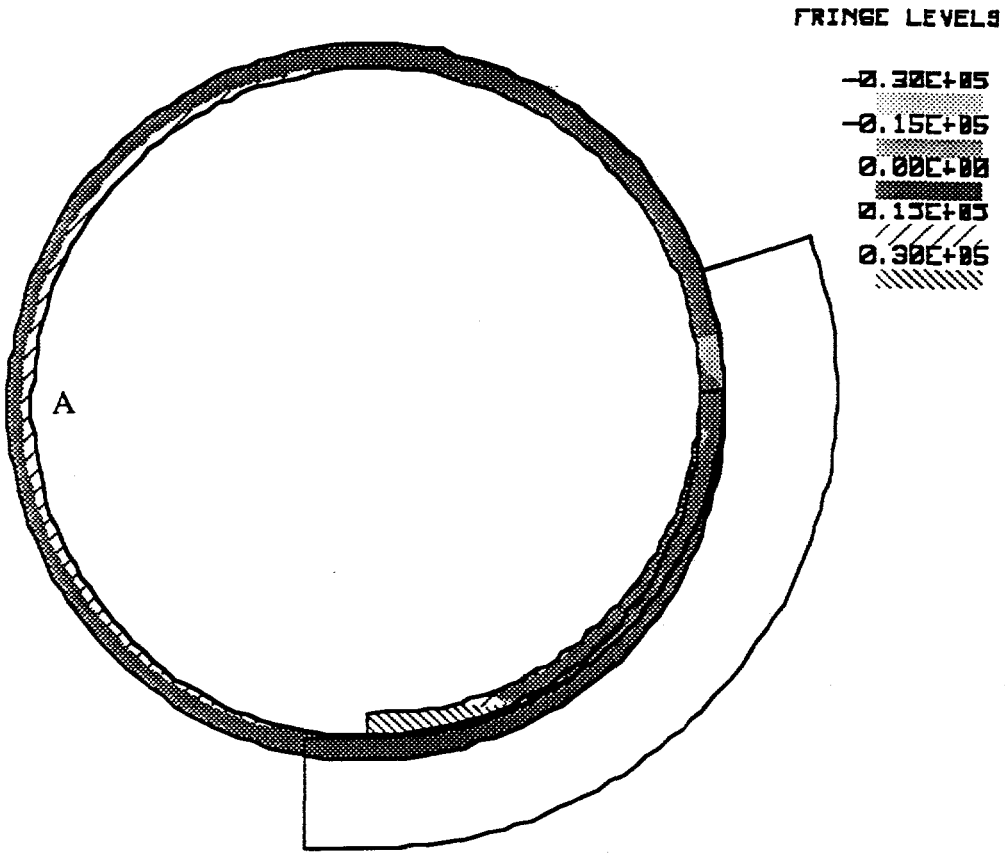

Figure 3.6 Maximum princpal stress fringes after prescribed displacement of 0.04 inches.

The stiffness of the chip can be determined from Castigliano's theorem. Figure 3.7 shows the centerline of a circular chip with an out-of-plane force P applied to its free end. Consider a typical cross-section of the chip at an angle θ from the free end. At this cross-section, there is an internal force (P), a bending moment (M), and a twisting moment (T). Strain energy is given by:

$$U = \int \frac{M^2 dS}{2EI} + \int \frac{T^2 dS}{2GJ} \tag{3.4}$$

where the moment M and the torque T are given by

$$M = P*R*SIN(\theta) \tag{3.5}$$

$$T = P*R*\{1-COS(\theta)\} \tag{3.6}$$

Applying Castigliano's theorem gives:

$$\delta = \frac{du}{dp} \tag{3.7}$$

where δ is the out-of-plane chip deflection given by the following relationship:

$$\delta = P*R^3*\Pi*(\frac{1}{EI} + \frac{3}{GJ}) \tag{3.8}$$

It is clear from this equation that the stiffness of the chip is highly dependent on its radius of curvature R. Therefore, a tightly-curled chip (small R) would require a large force to move it out-of-plane. In addition to the strength of the chip, friction between the chip and the flank face will also cause the chip to remain in contact with the tool. This is shown schematically in Fig. 3.8. As the chip approaches the tool, the frictional force will depend on the coefficient of friction and the normal force exerted by the chip. A stiffer chip will exert a larger normal force on the flank face, thereby providing a larger frictional force. Therefore, a more tightly-curled chip will be less likely to slide out-of-plane because of its large stiffness and the large frictional force acting on it. As a result, these chips will be more likely to develop the required stresses to cause them to fracture over a wide range of feeds and speeds.

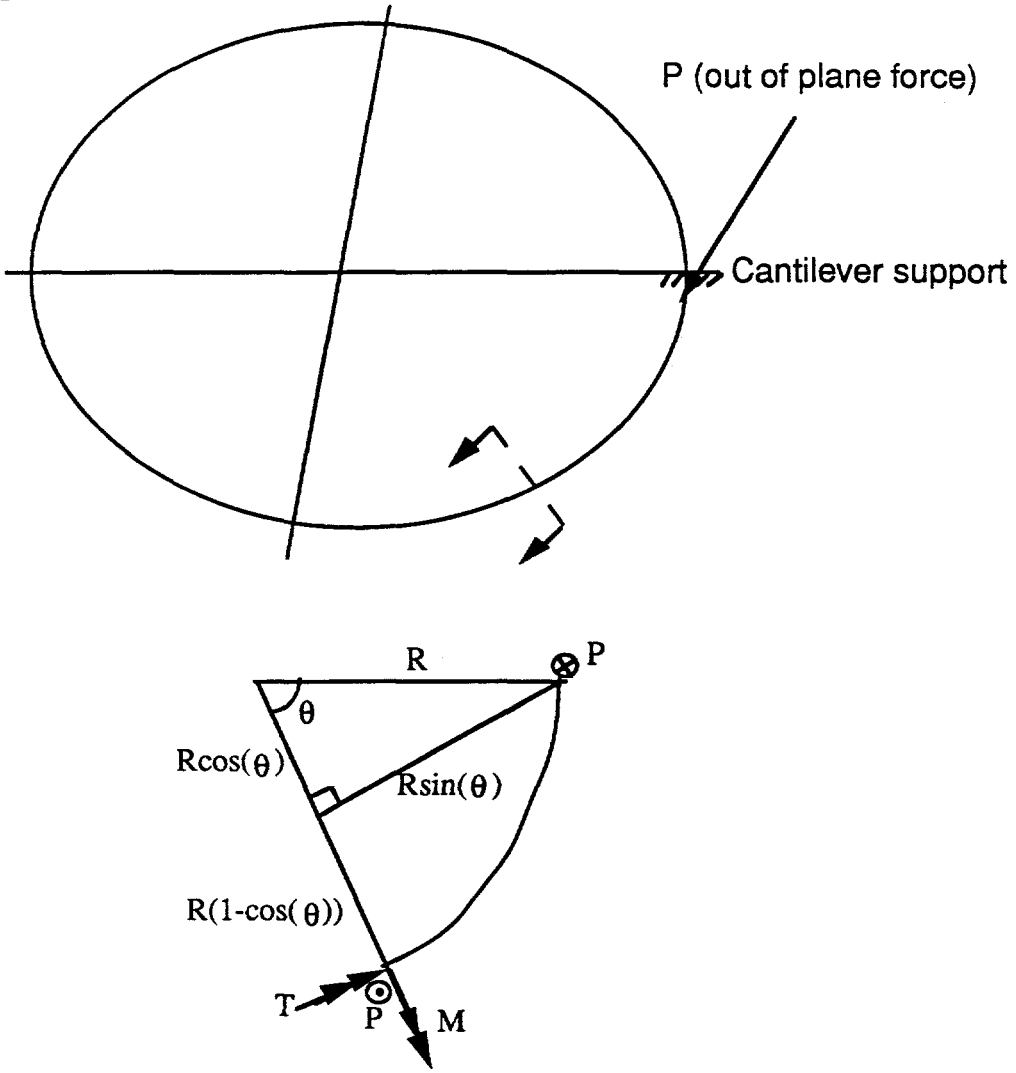

Figure 3.7 Chip centerline with out-of-plane loading

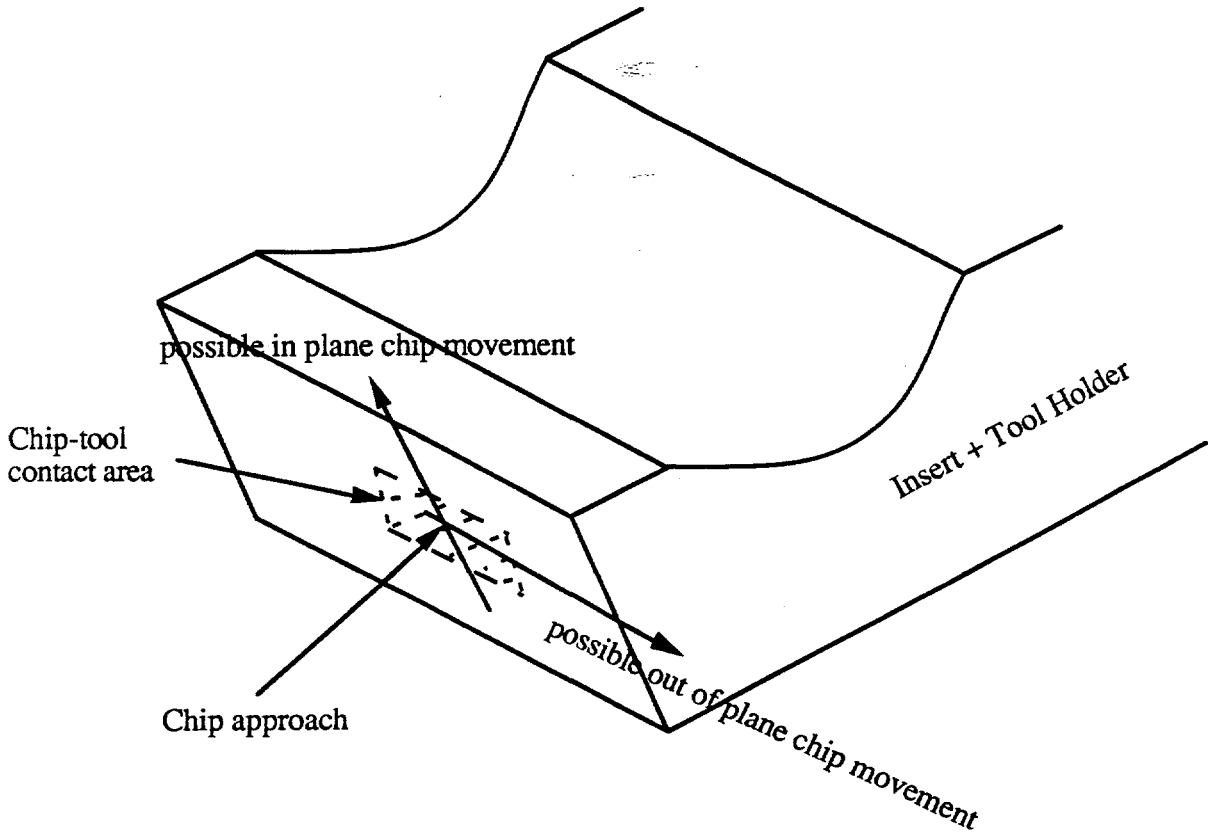

Figure 3.8 The chip-tool contact

4. Application of the Chip Breaking Models (Tasks 3 and 4)

The models described in the previous two sections were used to simulate chip formation and flow for 1020 steel using several grooved inserts. In conjunction with these simulations, experiments were performed to validate the cutting and chip breaking models. The following subsection describes the experimental procedures that were used. In Subsections 4.2 and 4.3, results from the models are compared with experimentally measured tool forces and chip geometry. Predicted chip temperature distributions are described in Subsection 4.4, and results from the chip breaking model are compared with experimental chip forms in Subsection 4.5.

4.1 Experimental cutting tests: techniques and apparatus

The cutting tests were conducted on a five horsepower Cincinnati Hydroshift lathe for 1020 steel using several groove-type inserts. The tools, feeds, and speeds used in the cutting tests are shown in Table 4.1. The workpiece was in the form of a 6 inch long tube with a 3 inch O.D. In order to achieve orthogonal cutting and plane strain conditions, the thickness of the tube was chosen to be 0.135 inch, which is much smaller than the diameter of the tube but much larger than the depth of cut (feed).

Figure 4.1 shows the tools that were tested. These are standard Carbolloy inserts that were chosen to provide a wide range of different chip forms for the attainable feeds and speeds with the available five horsepower lathe. The profile dimensions of the inserts are shown in Figure 4.2. These dimensions were determined by utilizing a Scherr Tumico (98-0002) tool maker's microscope. Before measuring, the grooved inserts were cut perpendicular to the cutting edge by a Buehler low speed saw with a diamond plate and then mounted in plastic through heating and pressing. Each dimension was measured ten times to obtain an average value of the land length, groove width, groove depth, and the raised back wall dimension.

Table 4.1. Summary of the cutting conditions

Grooved Inserts	TNMG 432E-26;-48;-68
Flat Insert	TNMA 432E
Rake Angle	-7^0
Clearance Angle	-7^0
Cutting Speed	40; 80; 120 in/sec
Feed	0.0032; 0.005; 0.007; 0.0091 in
Width of Cut	0.135 in
Cutting Edge Nose Radius	Sharp
Workpiece	C 1020
Lubrication	none

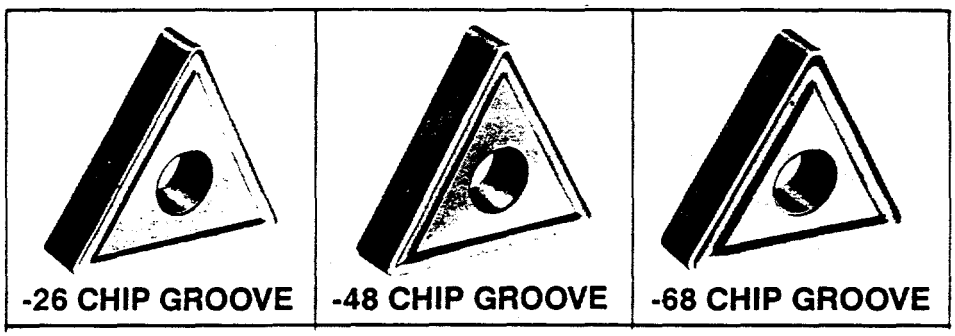

CHIP GROOVE NO.	I.C.	FEED RANGE (IPR*)	PROFILE	TOP VIEW
-26	.375″ .500″	.006-.012 .008-.016		
-48	.375″ .500″ .625″ .750″ 1.0″	.005-.014 .006-.020 .008-.024 .010-.028 .016-.045		
-68	.500″ .625″ .750″ 1.0″	.010-.028 .012-.032 .014-.040 .020-.050		

Fig. 4.1 Carbolloy cutting tool inserts

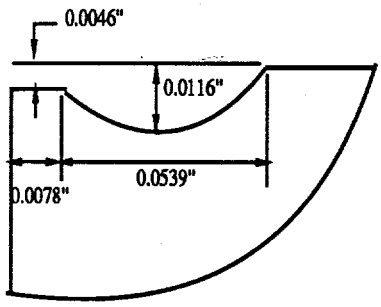

(a) TNMG 432E-26

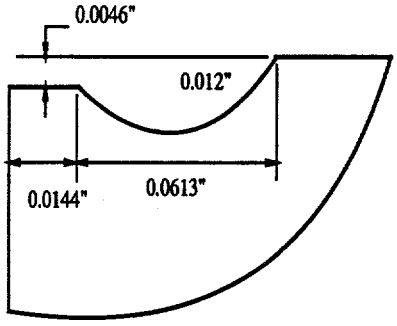

(b) TNMG 432E-48

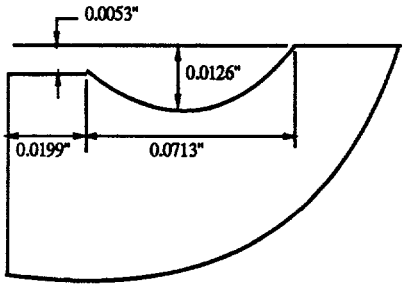

(c) TNMG 432E-68

Fig. 4.2 The measured dimensions of grooved inserts

In these experiments, the tool forces were measured with a Kistler (9257A) 3-component cutting force dynamometer on which the cutting tool was mounted. The output signals from the dynamometer were amplified through a Kistler (5001) charge amplifier and a Kistler (5211A) galvanometer amplifier before being recorded on a high speed SE Laboratories (M6150) ultraviolet recorder. The dynamometer was configured such that the three tool force components consisted of a component in the cutting direction (cutting force), a component perpendicular to the cutting direction (thrust force), and a component transverse to the cutting direction. The transverse force component was monitored to insure that it was negligible in order to maintain orthogonal cutting conditions. Once steady state cutting was reached, the measured forces remained relatively constant. However, it was found that in some cases, especially for higher feeds and lower speeds, the measured forces oscillated over a small range. For these cases, an average of the upper and lower forces was used as the measured force.

To measure the chip thickness, a method suggested by Boothroyd and Bailey was used for its simplicity and accuracy. In this method, the chip thickness can be obtained by weighing a known length of chip, such that

$$h_c = \frac{m}{lwr}$$

where h_c is the final chip thickness, m is the mass of the chip, l is the total length of the chip, w is the width of the chip, and r is the density of the chip. Note that in general the collected chips are curled due to the chip breaker inserts, which can present some difficulty in measuring the length. Therefore, the curled chips were straightened first and then the straightest part of the chip was used as the testing sample. The total length of the chip was found by adding together the individual samples.

The cutting experiments were performed for a range of cutting speeds from 40 in/sec to 120 in/sec, and feeds from 0.0032 to 0.0091 inch. In addition to the groove-type Carbolloy inserts, a flat insert of the same type and grade (570) was used for comparison.

4.2 Cutting forces

The measured and predicted cutting forces are shown in Figs. 4.3-4.5 for a flat tool and the TNMG-68 and TNMG-48 inserts, respectively. In general, the measured and the computed forces compare favorably. The best agreement was found at the lower feeds. At the higher feeds, the measured cutting force component is generally less than the computed results. It was found in the cutting tests that at the higher feeds, the chip would usually hit the uncut workpiece surface or the tool flank face prior to breaking. When this occurred, the cutting force component would decrease abruptly because an additional force was created in a direction opposite to the cutting direction. For lower feeds, this additional force was negligible because the chip is not very stiff. However, the chips are much stiffer for the higher

feeds, which causes the cutting force to vary. Similar agreement was found between the measured and computed thrust force component, as can be seen from Figs. 4.6 - 4.8.

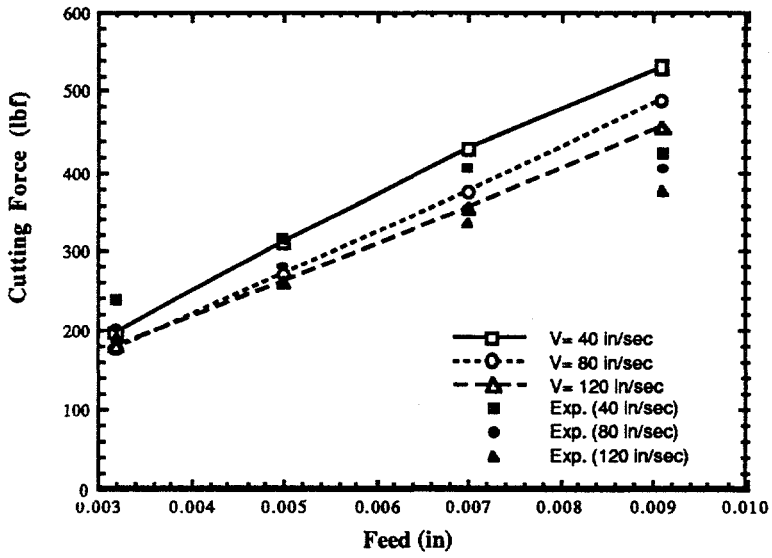

Fig. 4.3 Cutting force for flat insert

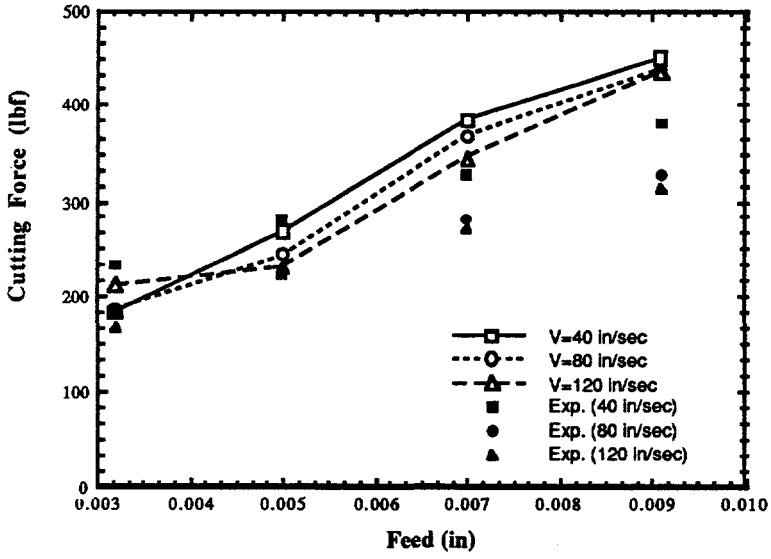

Fig. 4.4 Cutting force for C-68 insert

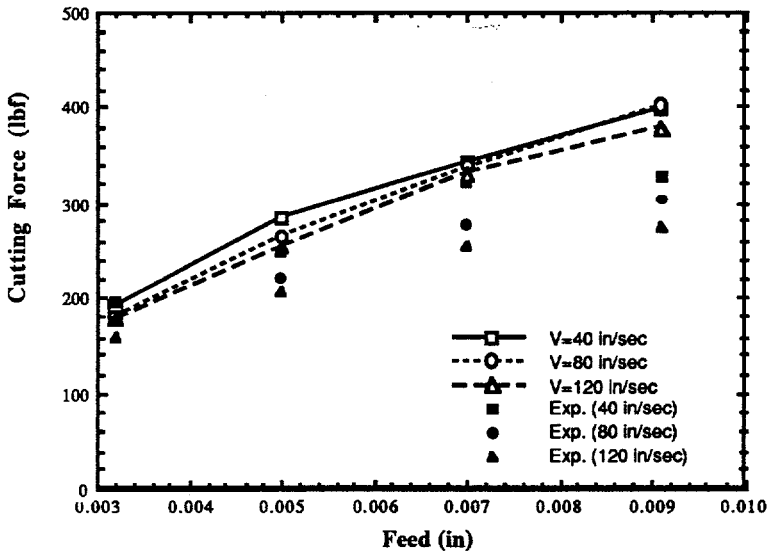

Fig. 4.5 Cutting force for C-48 insert

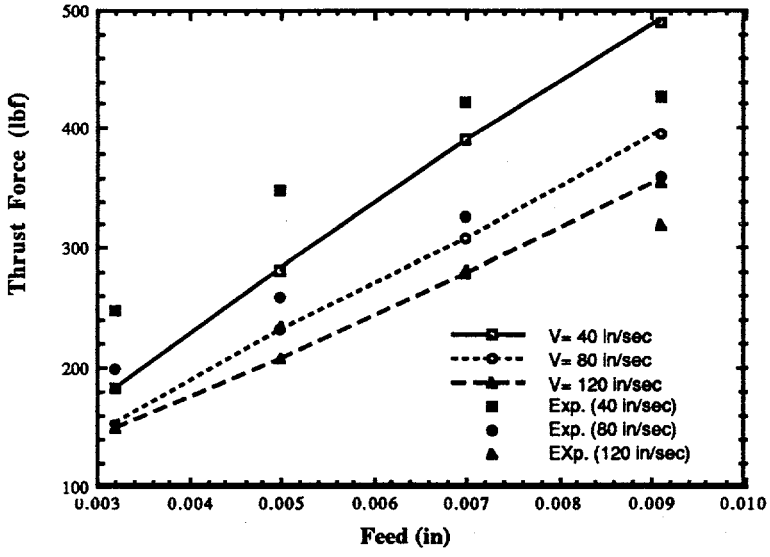

Fig. 4.6 Thrust force for flat insert

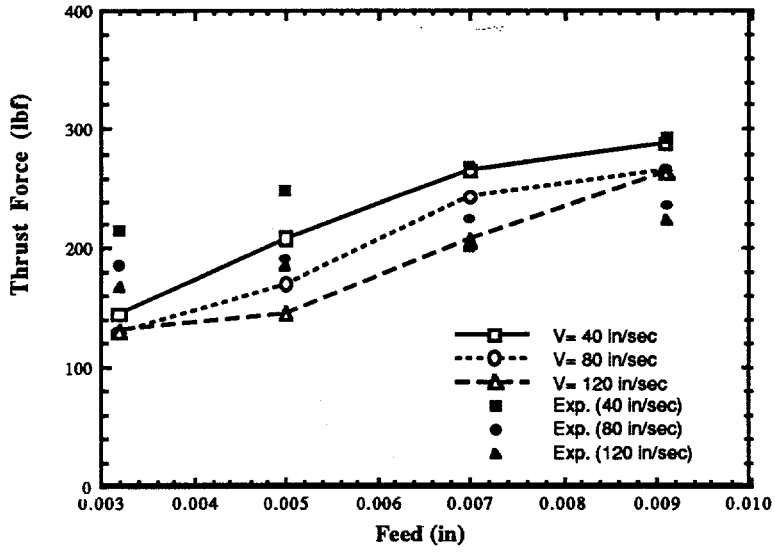

Fig. 4.7 Thrust force for C-68 insert

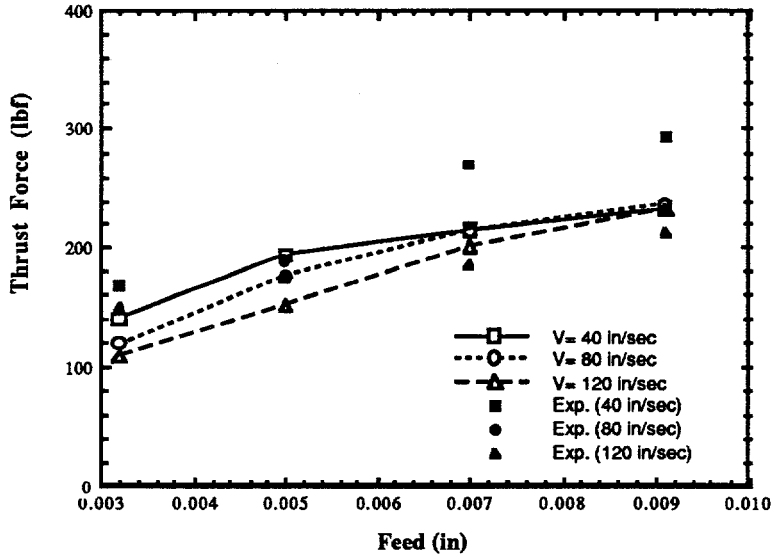

Fig. 4.8 Thrust force for C-48 insert

The computed cutting and thrust force components are shown in Figs. 4.9 and 4.10, respectively, as a function of cutting speed. In general, the forces do not vary appreciably with cutting speed for a given tool. However, there is a significant reduction in the forces for the different tools as the primary land is reduced. This result is consistent with other published research [6] that demonstrates that restricted contact length tools result in significantly lower tool forces.

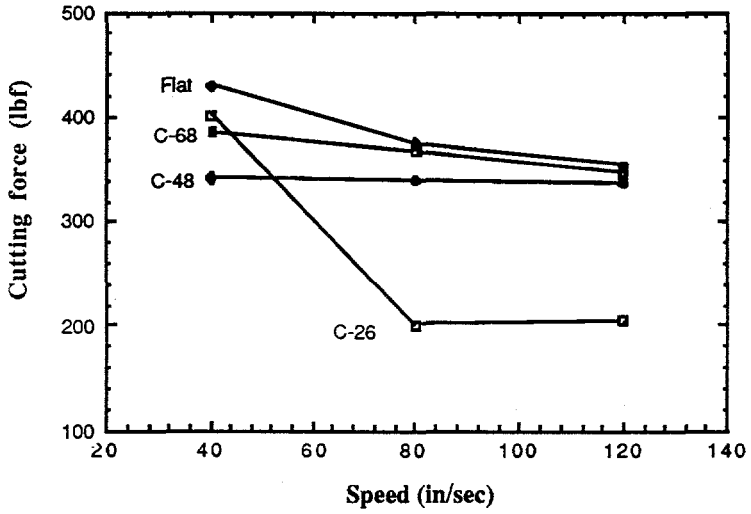

Fig. 4.9 Cutting force versus cutting speed
(feed = 0.007 in)

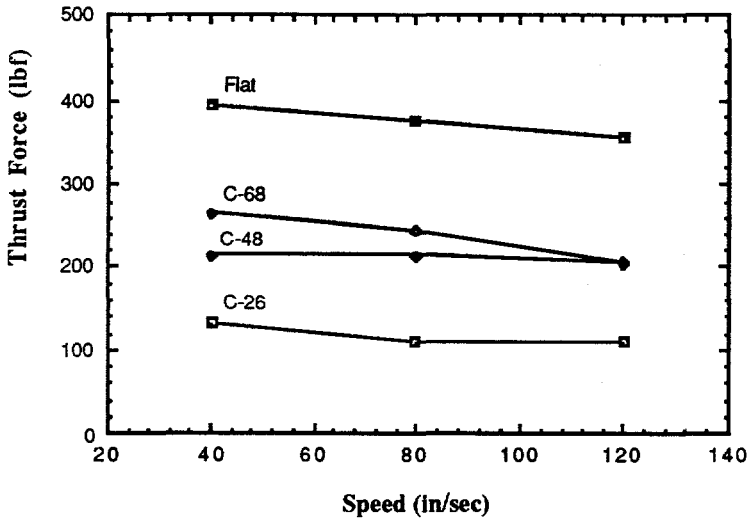

Fig. 4.10 Thrust force versus cutting speed
(feed = 0.007 in)

In contrast to cutting speed, the feed has an appreciable effect on the cutting and thrust force components, as shown in Figs. 4.11 and 4.12, respectively. It is interesting to note that the tool forces are less sensitive to the feed for tools with a smaller primary land. This is especially true for the smallest tool (C-26) for which the tool forces are nearly independent of the feed. This may be due to the fact that the tested feeds are approximately equal to the primary land length of 0.0078 inches for this insert. Therefore, there is less variation of the normal stress along the rake face for the small land inserts as compared to those with larger lands.

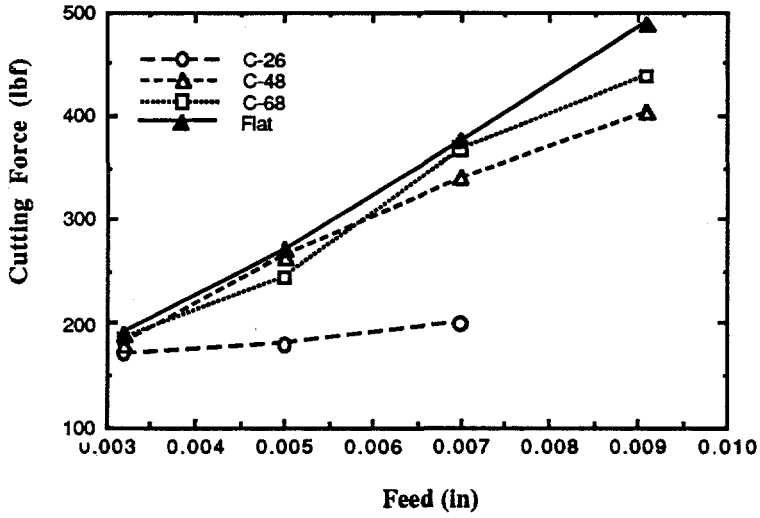

Fig. 4.11 Cutting force versus feed (speed = 80 in/sec)

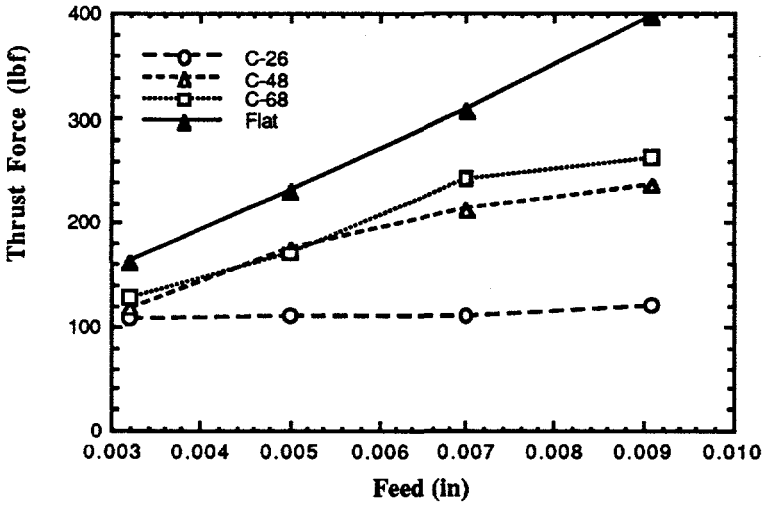

Fig. 4.12 Thrust force versus feed (speed = 80 in/sec)

4.3 Chip Geometry

Chip geometry is characterized by its thickness and radius of curvature. The cutting model can be used to predict the chip geometry and temperature distribution in the chip, workpiece, and tool. Tables 4.2 qnd 4.3 show the material and thermal properties that were used to simulate the cutting of 1020 steel with the Carbolloy inserts. Friction between the chip and the rake face of the flat insert was assumed to be 0.8, 0.7, and 0.6 for the three speeds tested, and 0.6, 0.5, and 0.4 for the grooved inserts, which reflect the fact that friction is reduced as the speed is increased. These friction coefficients were based upon measured tool forces.

Table 4.2 Material properties of steel 1020

Yield Stress	110 ksi
Density	0.284 lb/in^3
Specific Heat	0.1 Btu/lb-°F
Thermal Conductivity	27 Btu/hr-ft-°F

Table 4.3 Material properties of TNMG & TNMA tools

Density	0.539 lb/in^3
Specific Heat	0.045 Btu/lf-°F
Thermal Conductivity	30 Btu/hr-ft-°F

Figures 4.13-4.16 show the predicted chip geometry for all the inserts for a feed of 0.005 inch and speed of 40 in/sec. Significant changes in the chip geometry and chip temperatures occur as the length of the primary land is varied. As the contact length is reduced, the chip becomes thinner as well as more tightly curled. This can be seen in Figs. 4.17 and 4.18 which show the chip thickness for various tools as a function of speed and feed. For the flat and larger land inserts (C-48 and C-68), the thickness decreases with speed and increases with feed.

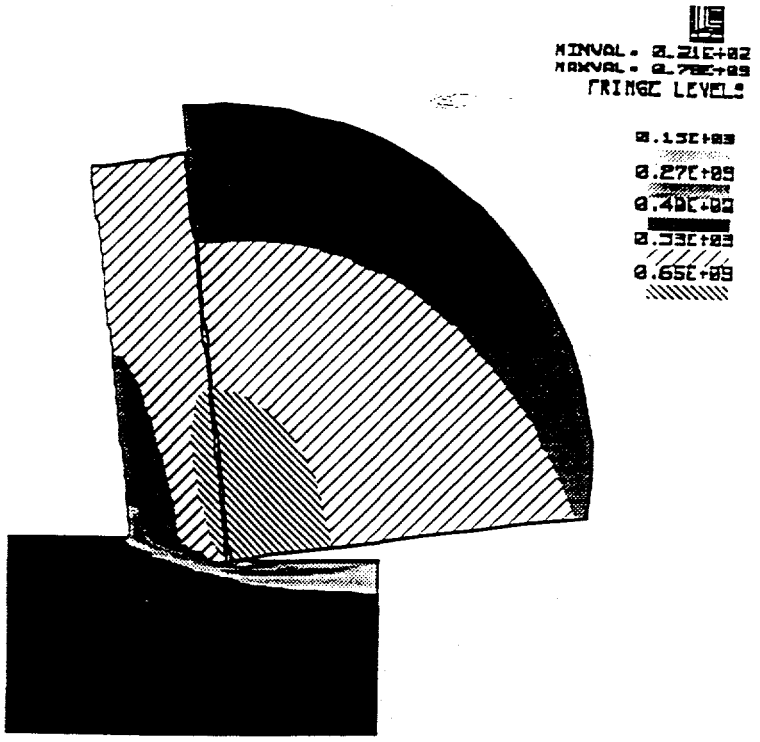

Fig. 4.13 Temperature distribution for flat insert
(feed = 0.005; V = 40 in/sec)

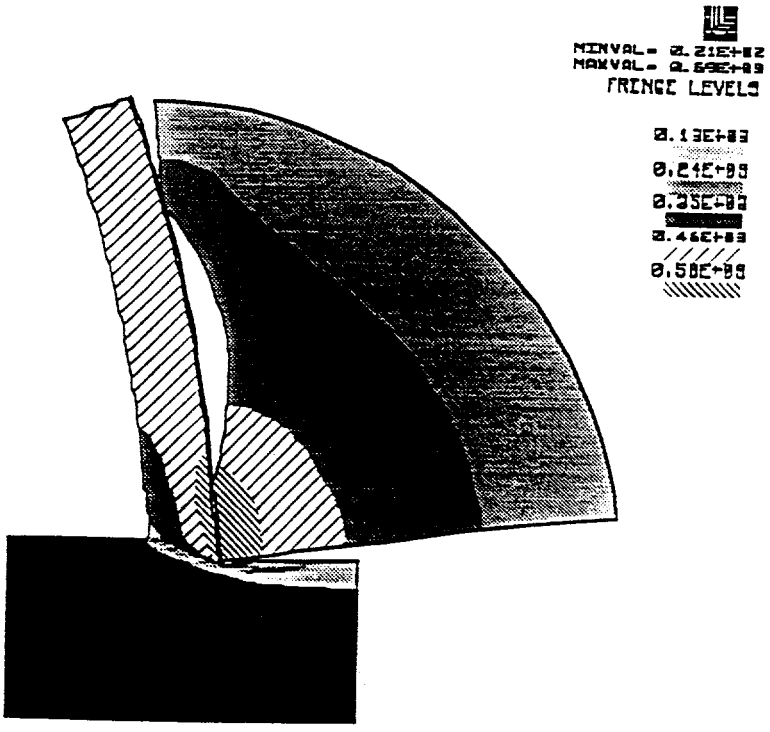

Fig. 4.14 Temperature distribution for C-68 insert
(feed = 0.005; V = 40 in/sec)

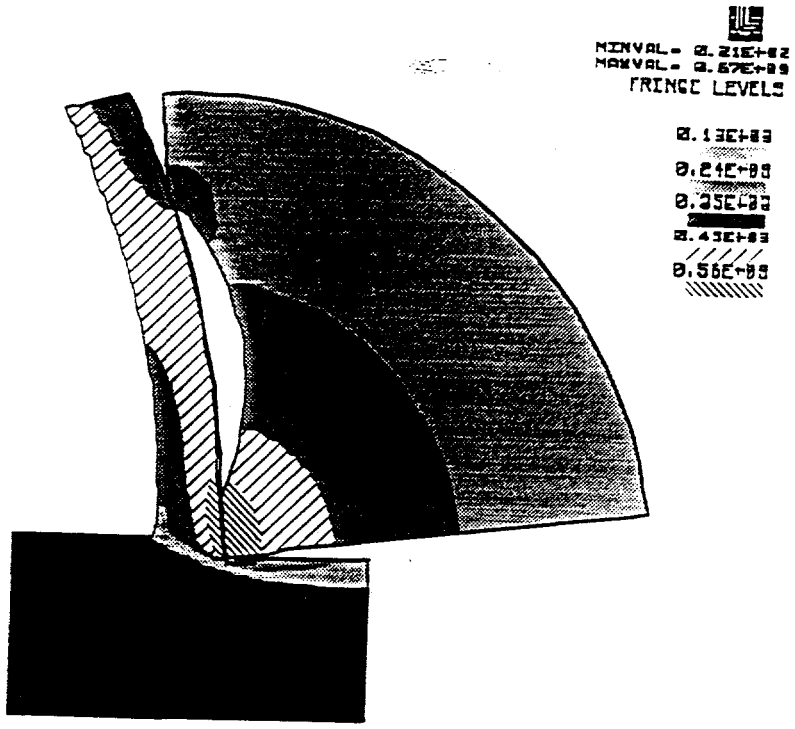

Fig. 4.15 Temperature distribution for C-48 insert
(feed = 0.005; V = 40 in/sec)

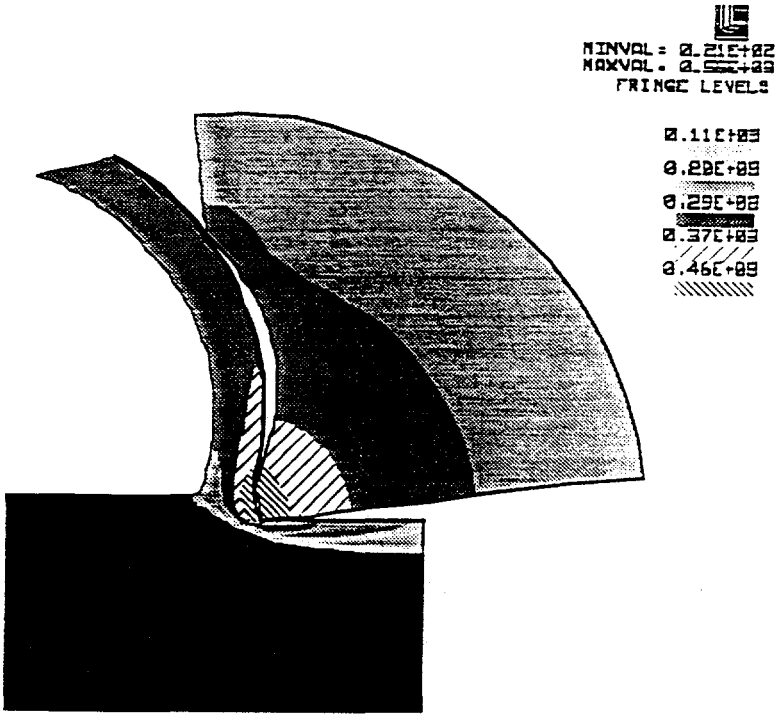

Fig. 4.16 Temperature distribution for C-26 insert
(feed = 0.005; V = 40 in/sec)

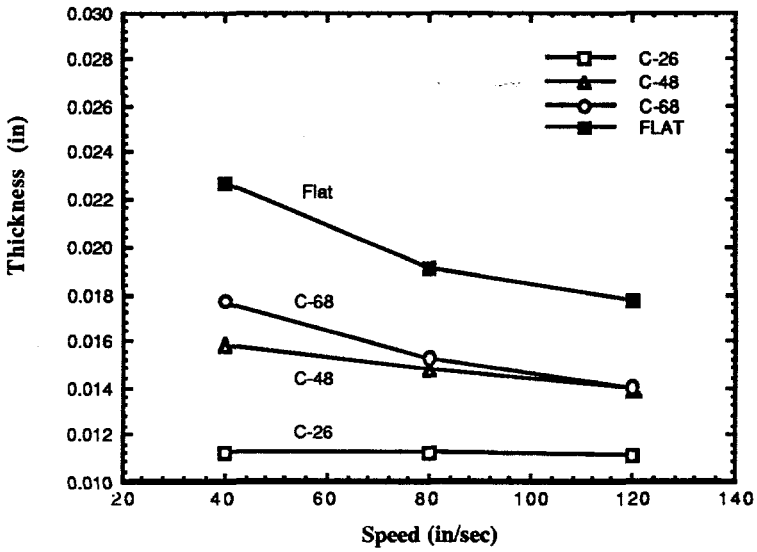

Fig. 4.17 Chip thickness versus speed (feed = 0.005 in)

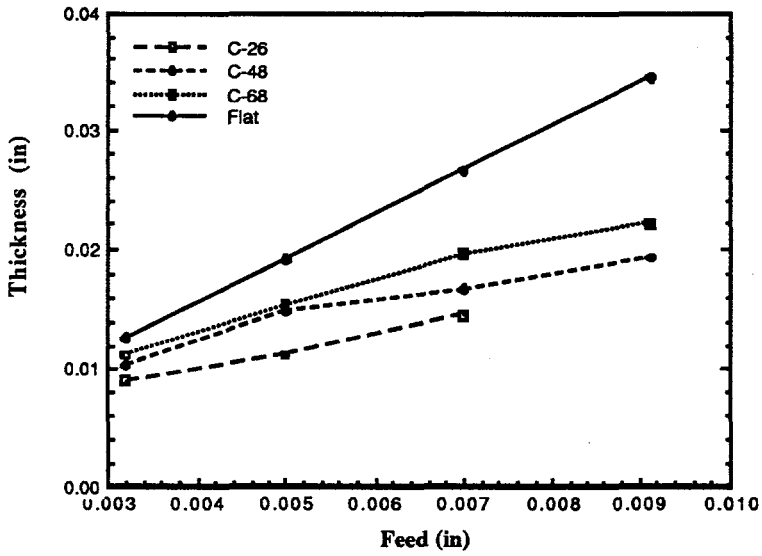

Fig. 4.18 Chip thickness versus feed (speed = 80 in/sec)

The chip thickness was measured using the technique described in a Section 4.1. Figures 4.19-4.22 show the chip thickness versus feed for the flat and three groove-type inserts, respectively. The computed chip thickness is also shown for comparison. In general, the agreement between the measured and computed thickness is very good, except for the flat insert at the largest feed of 0.0091 inch. This discrepancy is due to an observed side spread of the chip for the larger feeds. Strictly speaking, the appearance of side spread invalidates the assumption of orthogonal cutting.

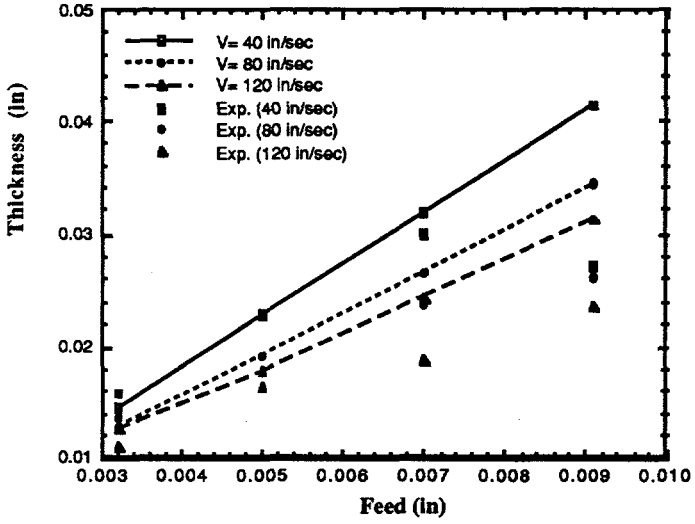

Fig. 4.19 Chip thickness versus feed for flat insert

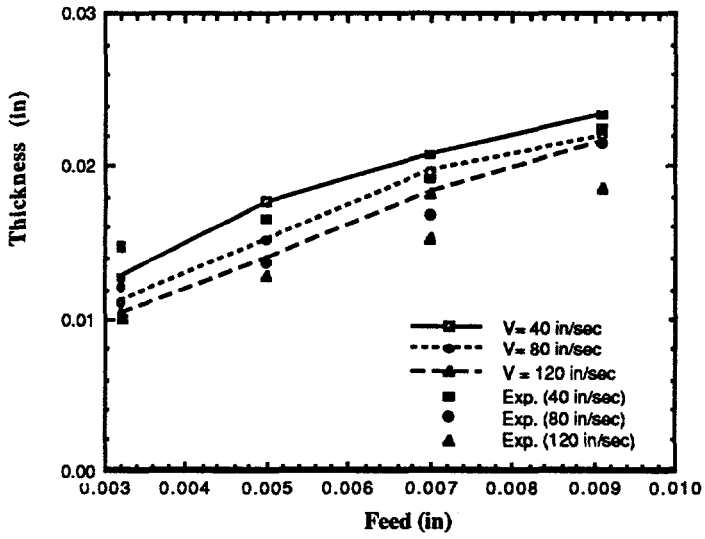

Fig. 4.20 Chip thickness versus feed for C-68 insert

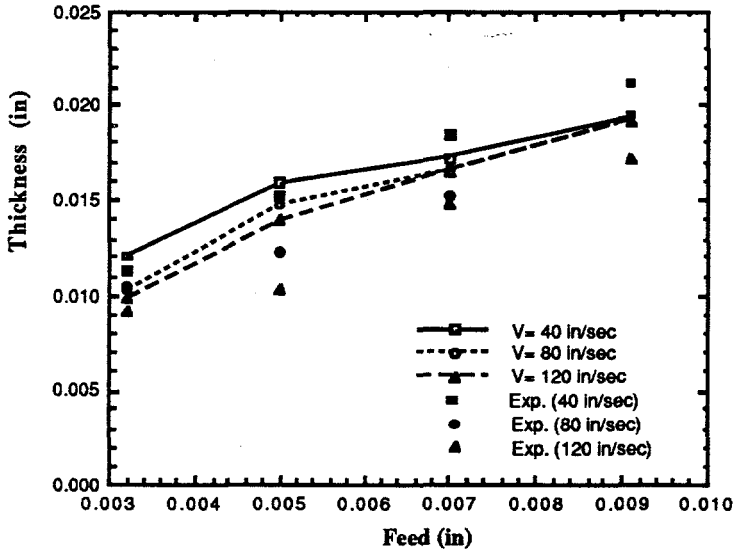

Fig. 4.21 Chip thickness versus feed for C-48 insert

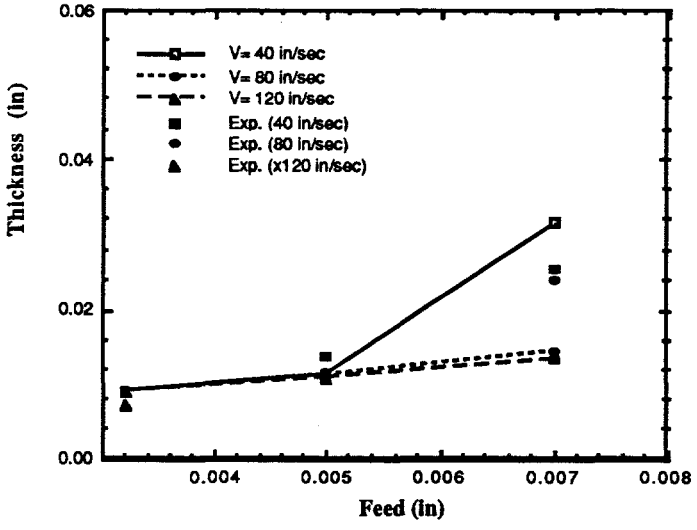

Fig. 4.22 Chip thickness versus feed for C-26 insert

The chip curvature was also computed with the model from the coordinates of three points on the surface of the predicted chip geometry. The curvature was found by averaging the radius of each side of the chip. It was found that the curvature is largely independent of the speed, as shown in Fig.4.23. However, there is a strong dependence of the curvature on the feed, as can be seen in Fig. 4.24 for a cutting speed of 120 in/sec for various inserts.

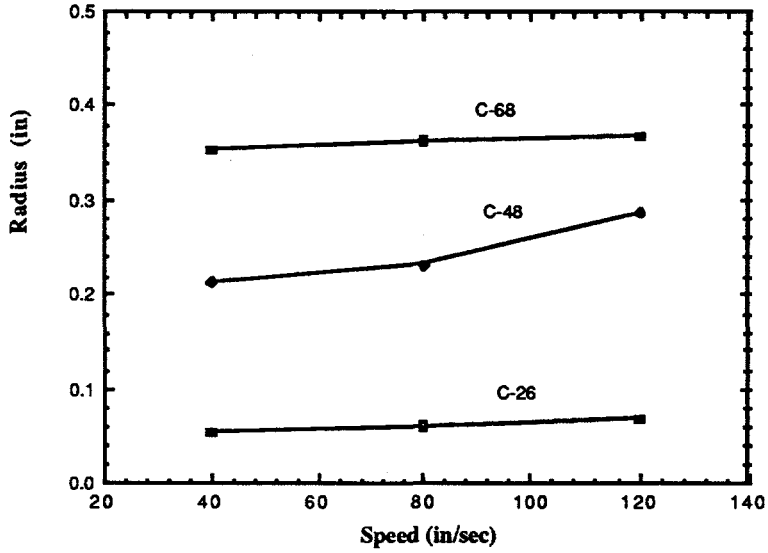

Fig. 4.23 Chip radius versus speed (feed = 0.005 in)

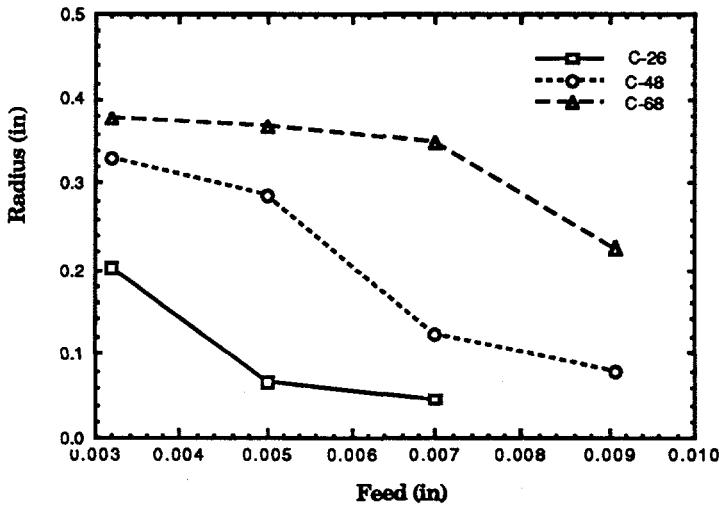

Fig. 4.24 Chip radius versus feed (speed = 120 in/sec)

For the speeds and feeds selected, it was found that the natural contact length was always greater than the restricted contact length of the inserts. This can be seen in Fig.4.13-4.16 where the chip is in full contact with the primary land of each insert. Therefore, the primary land length controls the chip/tool contact. It is interesting to plot the curvature as a function of the ratio of the land length to the feed, as shown in Fig. 4.25 Although this curve has been derived from the computed curvatures of various inserts, there is nearly a linear relationship between the curvature and this ratio. Similar results are apparent from Figs. 4.26 and 4.27, which show the curvature for two different speeds.

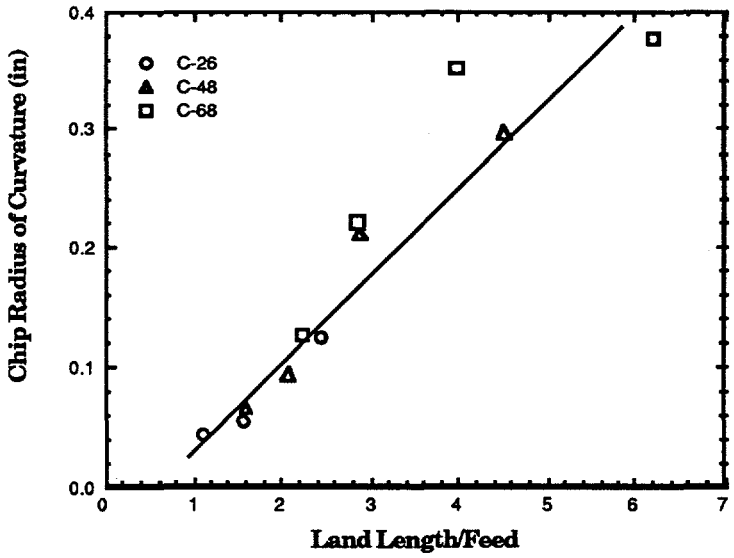

Fig. 4.25 Radius versus land length/feed for speed of 40 in/sec

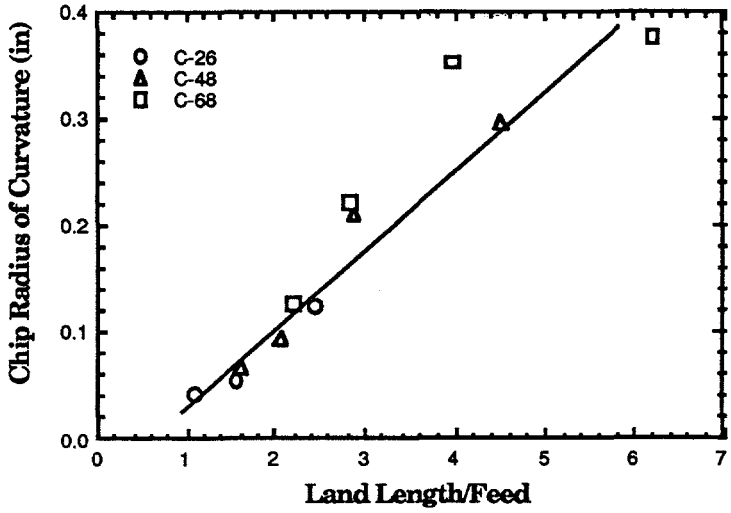

Fig. 4.26 Radius versus land length/feed for speed of 80 in/sec

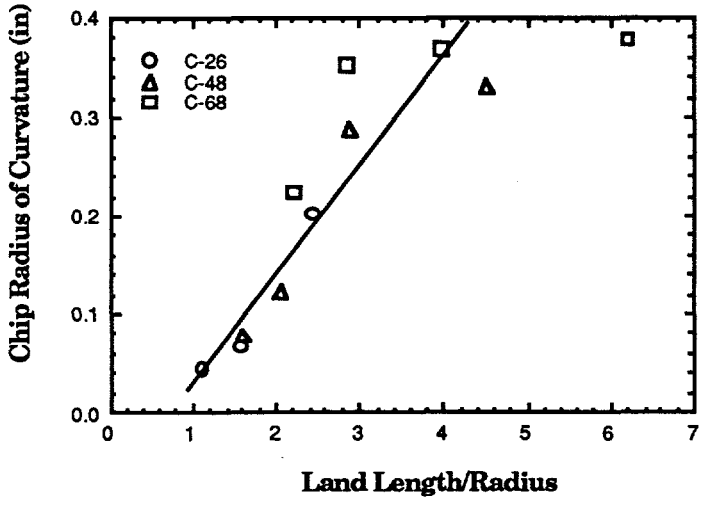

Fig. 4.27 Radius versus land length/feed for speed of 120 in/sec

The dependence of the chip thickness and curvature on the cutting conditions and insert geometry is important because the strain in the chip is proportional to the ratio of the chip thickness to the curvature (equation (3.1)). Therefore, the strain is highly dependent on the insert geometry. This ratio was computed for each of the inserts as shown in Figs. 4.28-4.30 for the three tested speeds. A horizontal line is also plotted in each of these figures, which represents the experimental value of the ratio necessary for chips to break.

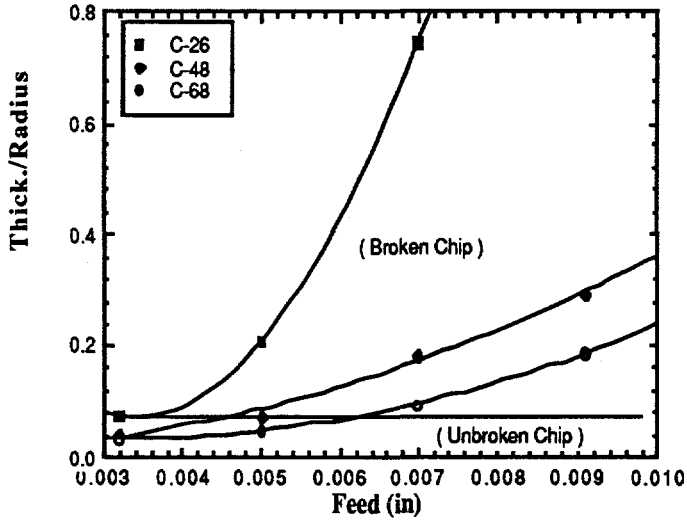

Fig. 4.28 Thickness/radius vs. feed for speed of 40 in/sec

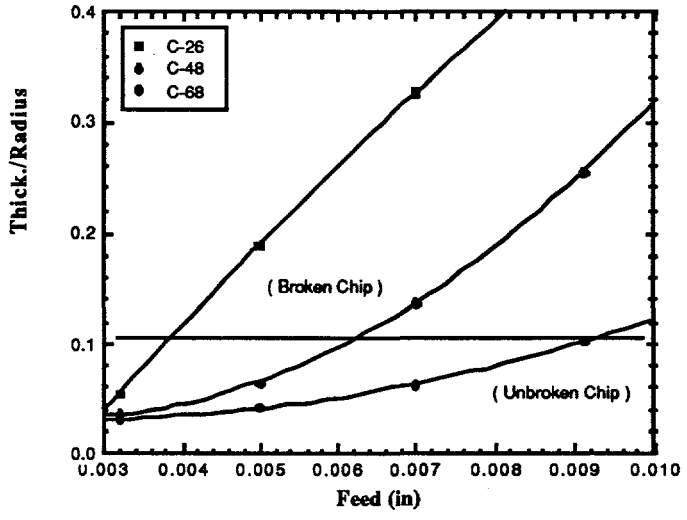

Fig. 4.29 Thickness/radius vs. feed for speed of 80 in/sec

For example, it was found that the chip thickness/radius ratio must exceed 0.1 for a speed of 80 in/sec to break chips. Note that as the speed is increased, the ratio needed for chips to break is increased. However, the thickness/radius ratio decreases as the speed is increased for any tool as shown in Fig. 4.31. Therefore, it becomes more difficult to break chips as the speed is increased.

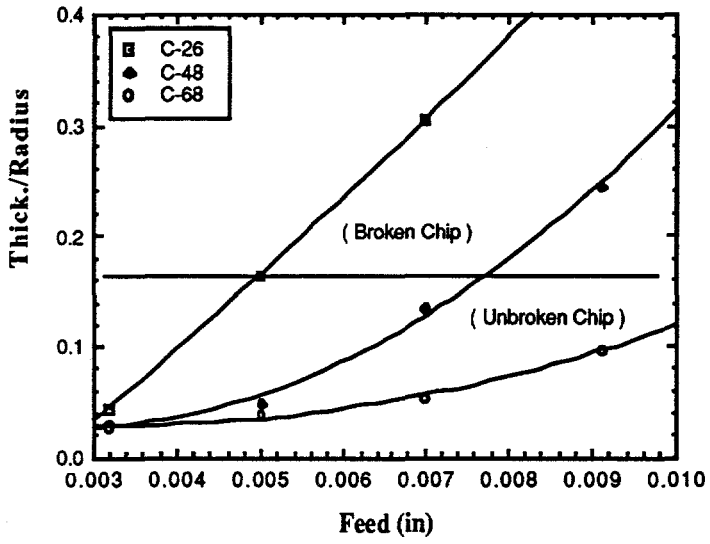

Fig. 4.30 Thickness/radius vs. feed for speed of 120 in/sec

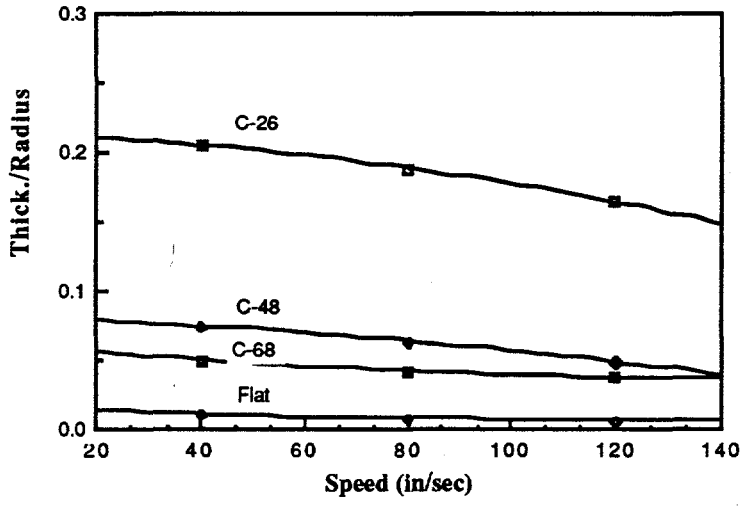

Fig. 4.31 Thickness/radius vs. feed for feed of 0.005 in

These results can be used to predict the chip breakability of a tool. As the speed is increased, the potential of an insert for breaking chips is reduced. An insert with a smaller land will have a higher thickness/radius ratio so that it will be more likely to break chips over a wider range of speeds and feeds. This can be seen in Fig. 4.32 which shows the thickness/radius as a function of land length/feed. As the feed is decreased, the thickness/radius ratio is insensitive to the cutting speed. However, the critical thickness/ radius ratio increases significantly as the speed is increased. Recall that the critical thickness/radius ratio, which is a measure of the mechanical strength of the chip, was derived from the experimental cutting tests. Therefore, this figure indicates that the mechanical strength of the chip increases with speed, thereby making it more difficult to break chips as the speed is increased. This could be a result of the chip becoming more ductile as the temperature increases at the higher cutting speeds.

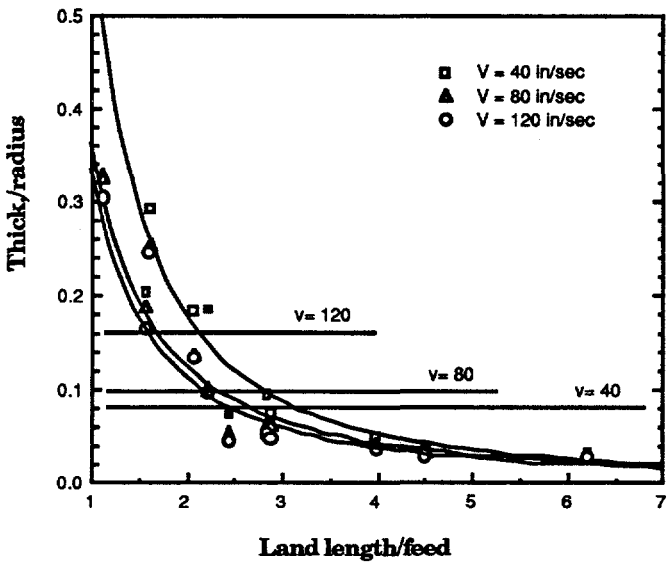

Fig. 4.32 Thickness/radius vs. land length/feed of different speeds

4.4 Chip temperatures

The predicted temperature distributions in the chip, workpiece, and tool are shown in Figs. 4.13-4.16 for the various inserts. The highest temperature always occurs along the tool rake face. The maximum temperature was found to occur at some distance from the cutting edge along the rake face for both the flat and the grooved inserts. For the grooved inserts, the highest temperature was near the lower corner of the groove.

Temperatures in the chip and tool are dramatically effected by the insert geometry. Figures 4.33 and 4.34 show the maximum temperature as a function of cutting speed for the various tools for two feeds. As expected, the temperature increases with the speed and feed. An exception to this trend occurs for the C-26 insert at the lowest speed of 40 in/sec and the feed of 0.007 inch. In this case, the land length is approximately equal to the feed which causes the chip to flow into the groove. This can be seen in Fig. 4.35 As a consequence, the chip thickness and the generated frictional heat increase, which results in a dramatic rise in the temperature.

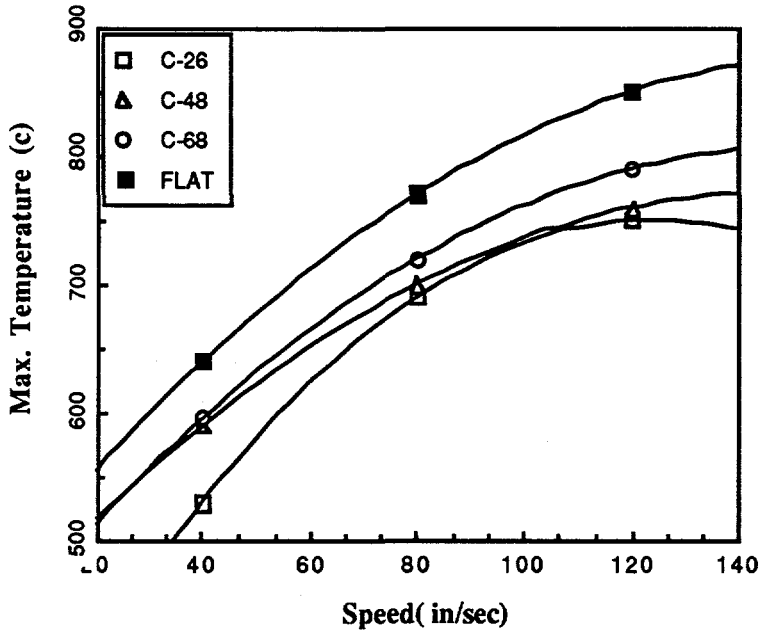

Fig. 4.33 Maximum temperature vs. speed for feed of 0.0032 in

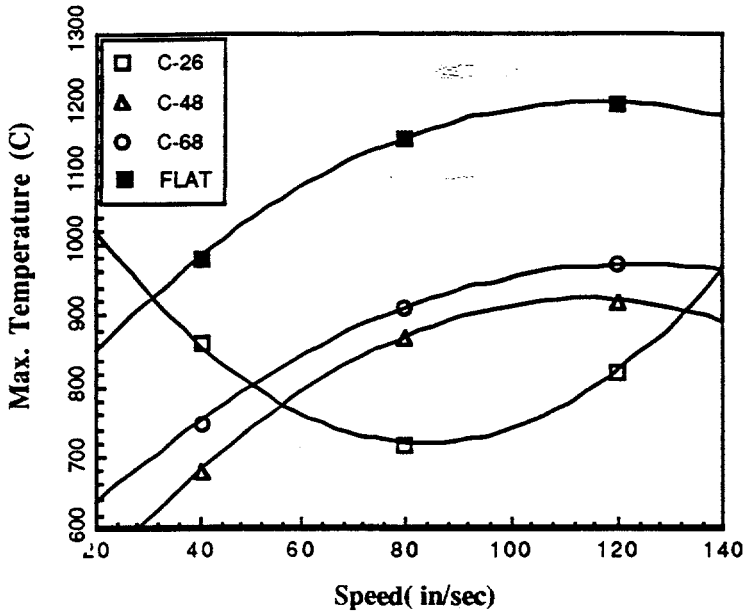

Fig. 4.34 Maximum temperature vs. speed for feed of 0.007 in

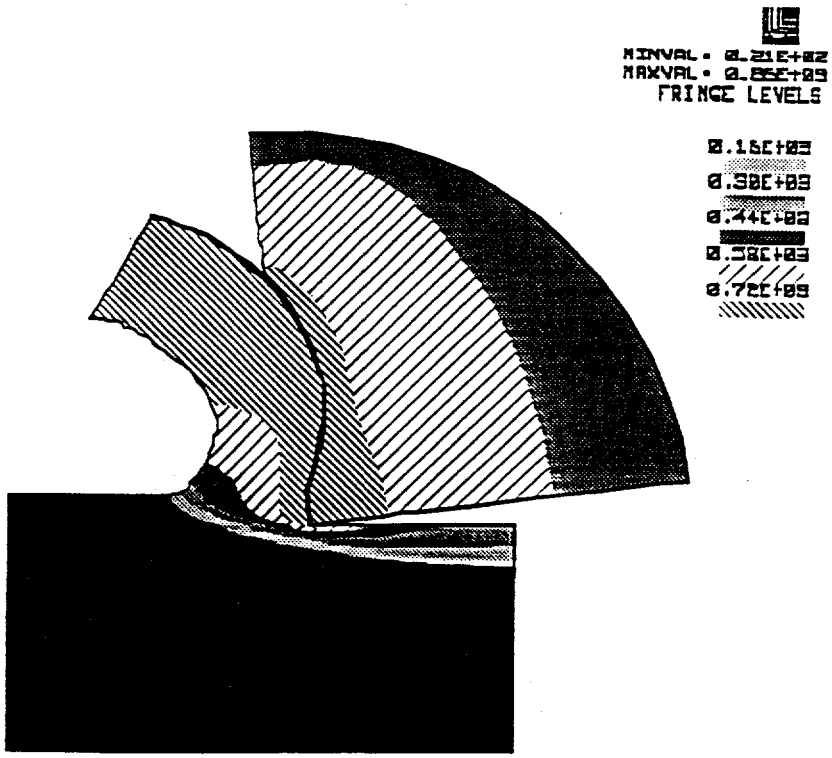

Fig. 4.35 Temperature distribution for C-26 insert
(feed = 0.007 in; V = 40 in/sec)

4.5 Chip breaking tests and model results

A wide range of chip forms was obtained for the tested feeds and speeds. Figure 4.36 (a) shows the speeds and feeds for which broken chips were obtained for the C-26 insert. Figure 4.36 (b) shows the corresponding chip forms that were obtained. As expected, chips were more likely to break at the higher feeds and lower speeds.

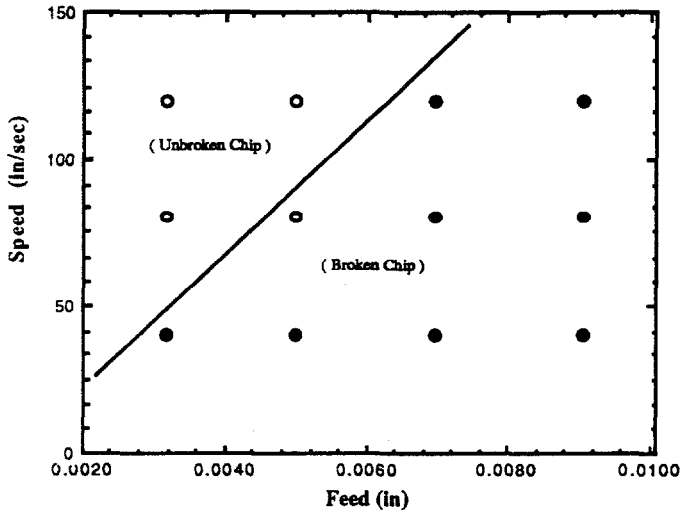

Fig. 4.36 (a) Chip forms in various conditions for C-26 insert

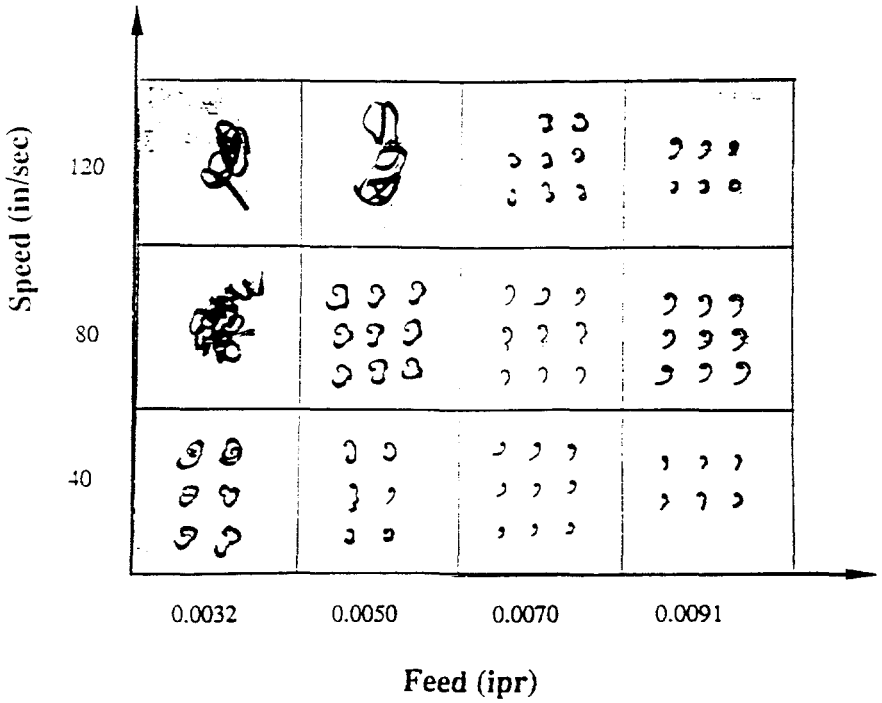

Fig. 4.36 (b) Chip forms for C-26 insert

Figures 4.37 and 4.38 show similar results for the C-48 and C-68 inserts, respectively. Note that the range of feeds and speeds for which chips will break increases as the primary land length decreases. For example, chips will break for a feed of 0.007 inch for the C-68 insert for only one tested speed (40 in/sec), whereas broken chips were obtained for the C-26 insert for all tested speeds.

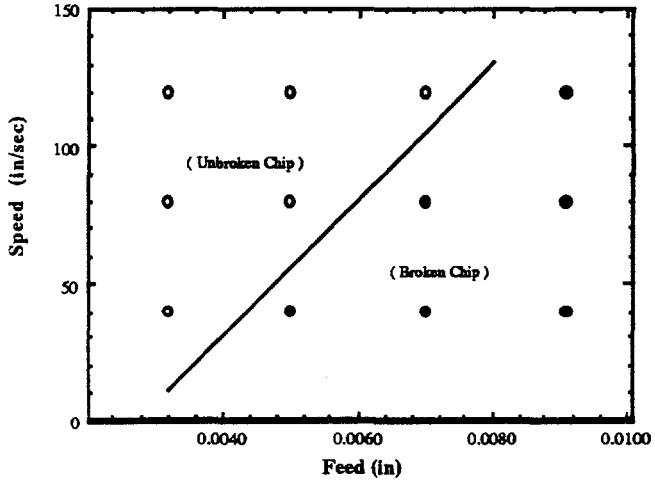

Fig. 4.37 (a) Chip forms in various conditions for C-48 insert

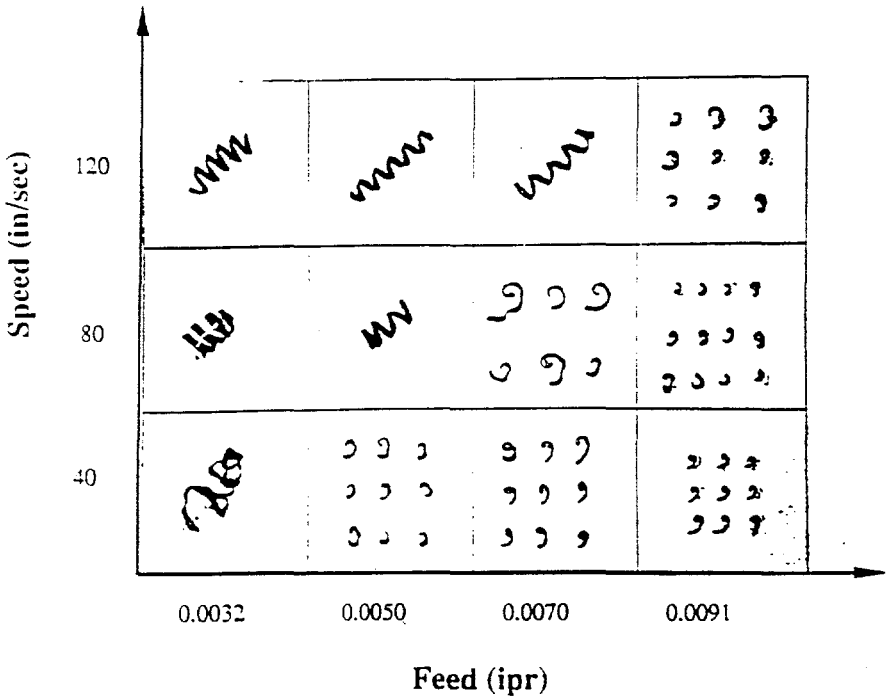

Fig. 4.37 (b) Chip forms for C-48 insert

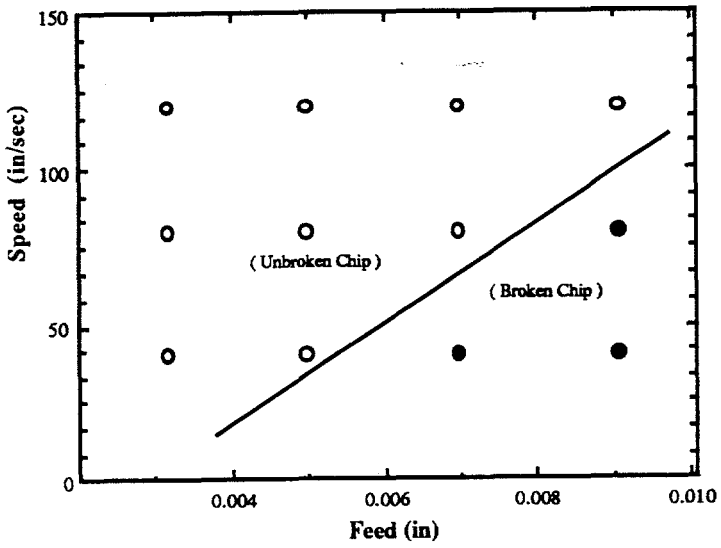

Fig. 4.38 (a) Chip forms in various conditions for C-68 insert

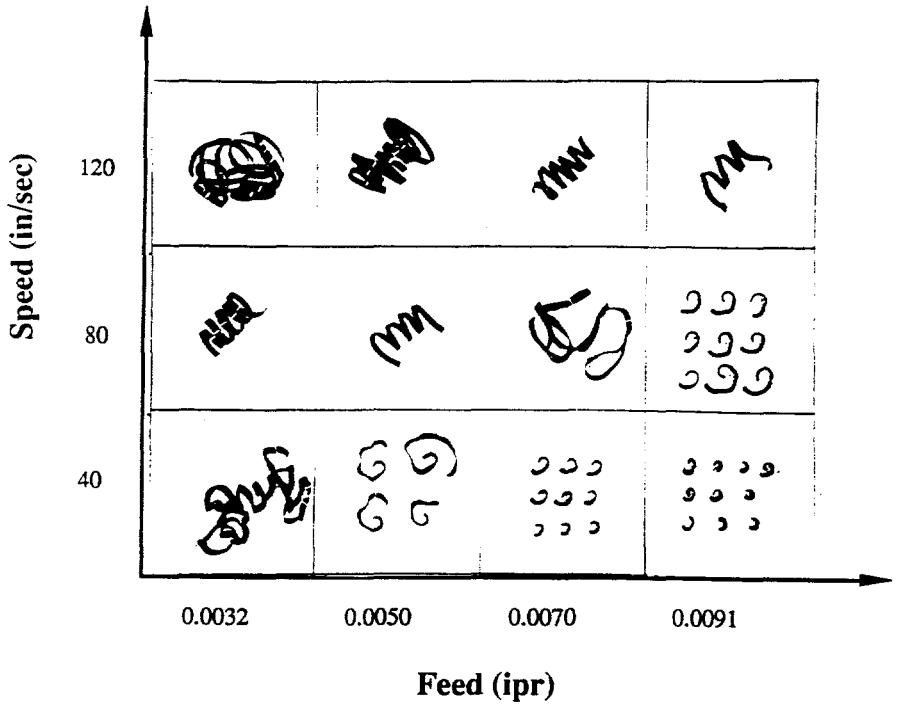

Fig. 4.38 (b) Chip forms for C-68 insert

The chip geometry is characterized by its thickness and radius of curvature. As discussed previously, the chip geometry depends on the speed, feed, and insert geometry. The cutting model can be used to determine the initial chip geometry. The stress distribution in the chip after it leaves the groove can then be found from the NIKE2D-based chip breaking model discussed in Section 3.

Figure 4.39 shows the chip geometry corresponding to the C-48 insert for a speed of 40 in/sec and a feed rate of 0.0032 in/rev. The radius of curvature and chip thickness were determined from the cutting model. Figure 4.40 shows the chip after point A has been displaced 0.1 inch. This displacement was required for the longitudinal stress to reach a value of 30,000 psi at point B. Note that the maximum principal stress is a maximum at point B, which indicates that the chip will fracture at this point. Figure 4.41 shows an enlargement of this region, where the stress is tensile on the inside surface. Fracture of the chip at this location was consistent with the experimental chip breaking tests.

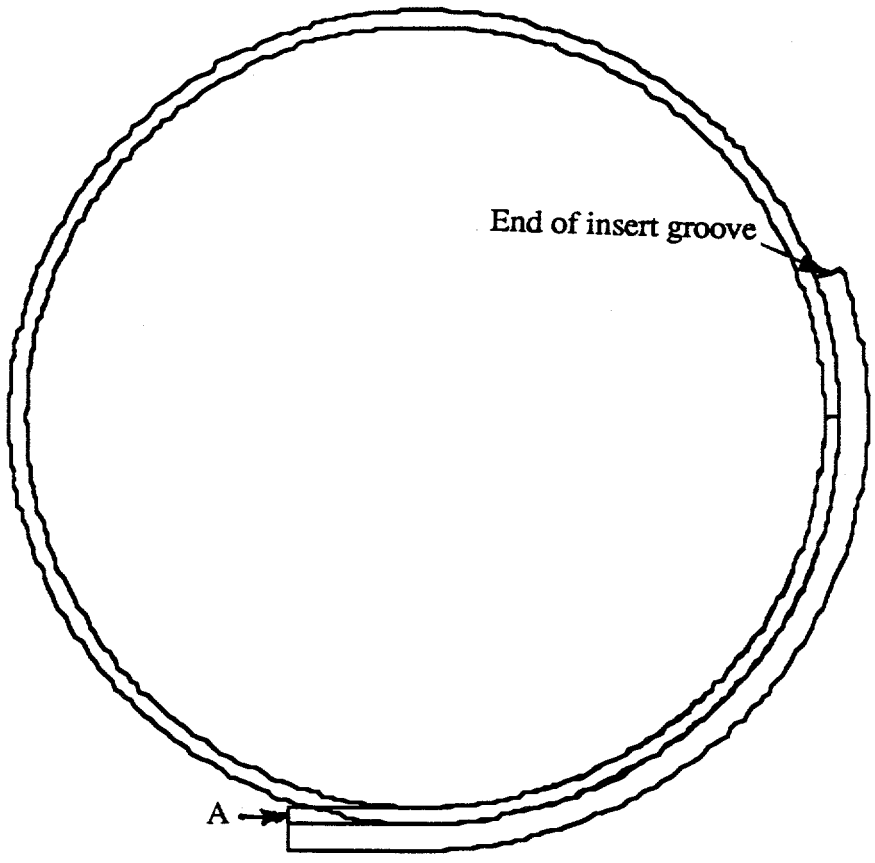

Fig. 4.39 Initial chip geometry for C-48 groove for feed of 0.0032 in/rev and cutting speed of 40 in/s .

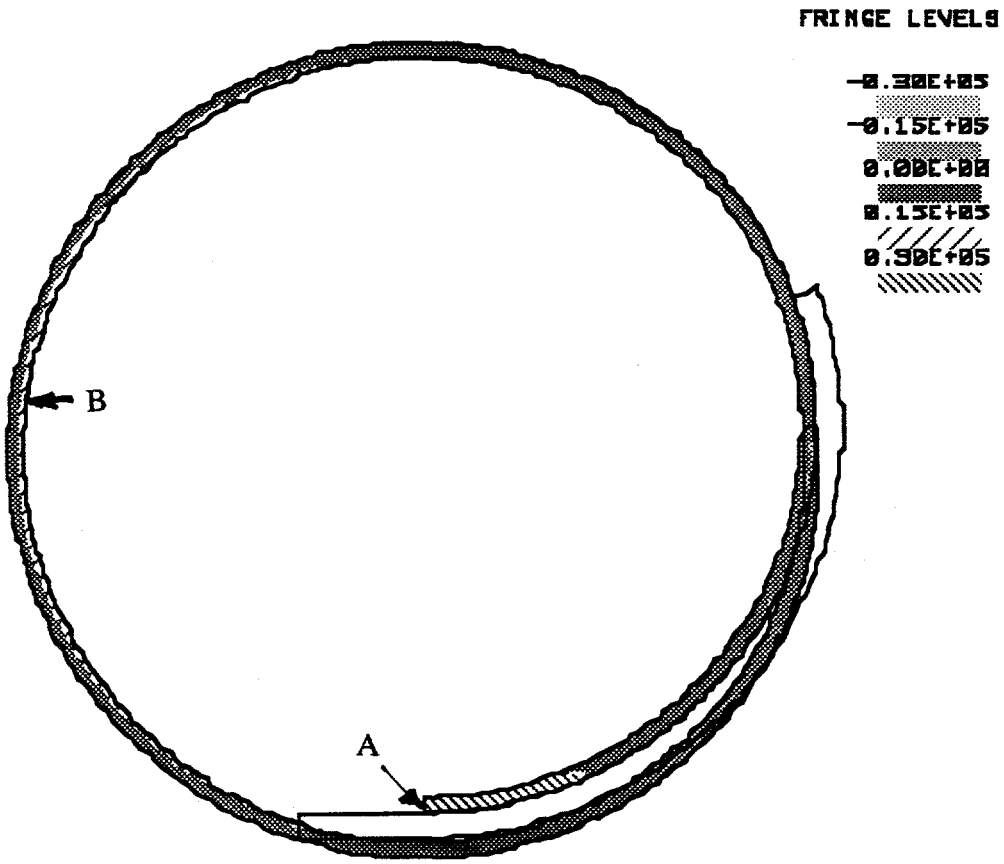

Fig. 4.40 Final chip geometry and maximum principal stress fringes for C-48 groove for feed of 0.0032 in/rev and cutting speed of 40 in/s .

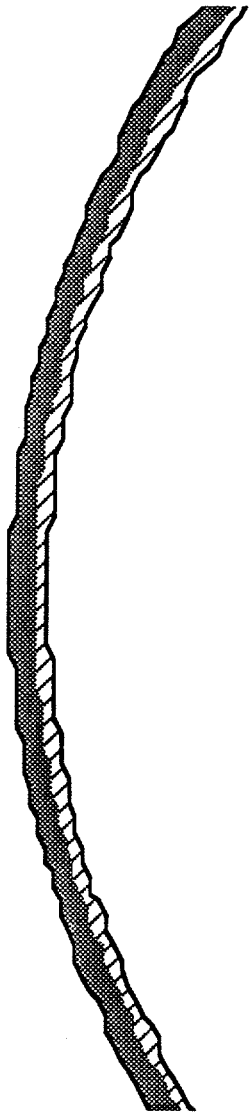

Fig. 4.41 Maximum principal stress fringes near point B in Figure 4.40

Similar results are shown in Fig. 4.42 for the C-48 insert for a larger feed rate of 0.0092 in/rev. Compared to the smaller feeds, this larger feed results in a thicker and more tightly-curled chip. As shown in Fig. 4.43, the largest maximum principal stress of 30,000 psi occurs again at point B, but for a much smaller prescribed displacement of 0.003 inch. The much reduced displacement results for the higher feed because the chip is much stiffer.

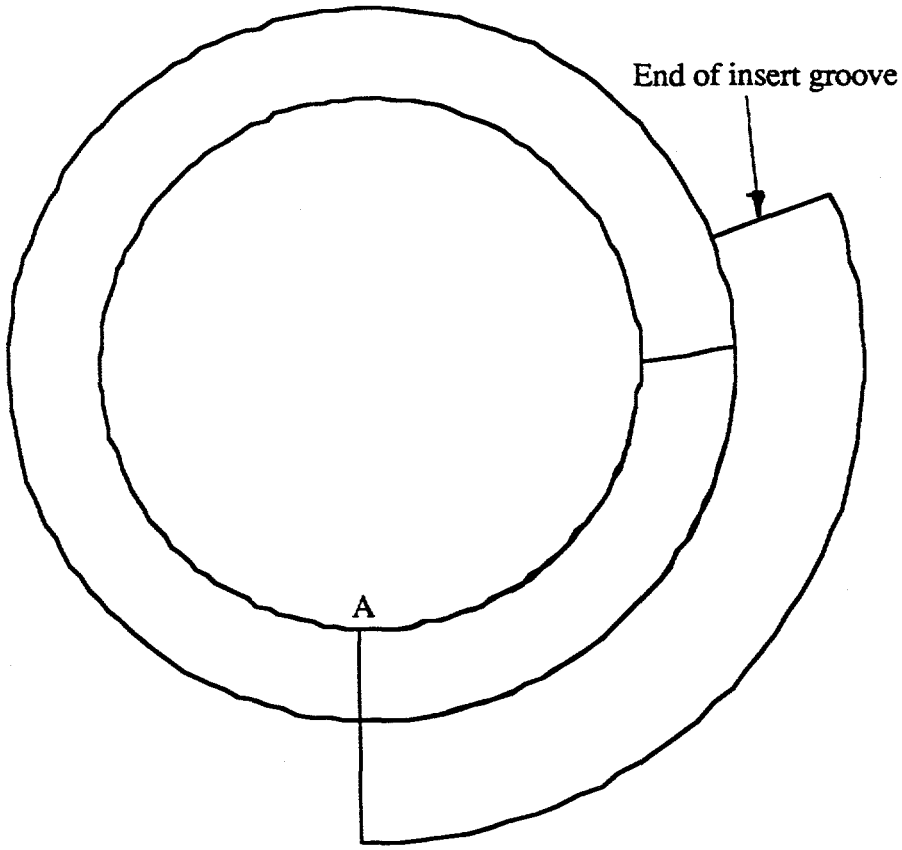

Fig. 4.42 Initial chip geometry for C-48 groove for feed of 0.0091 in/rev and cutting speed of 40 in/s .

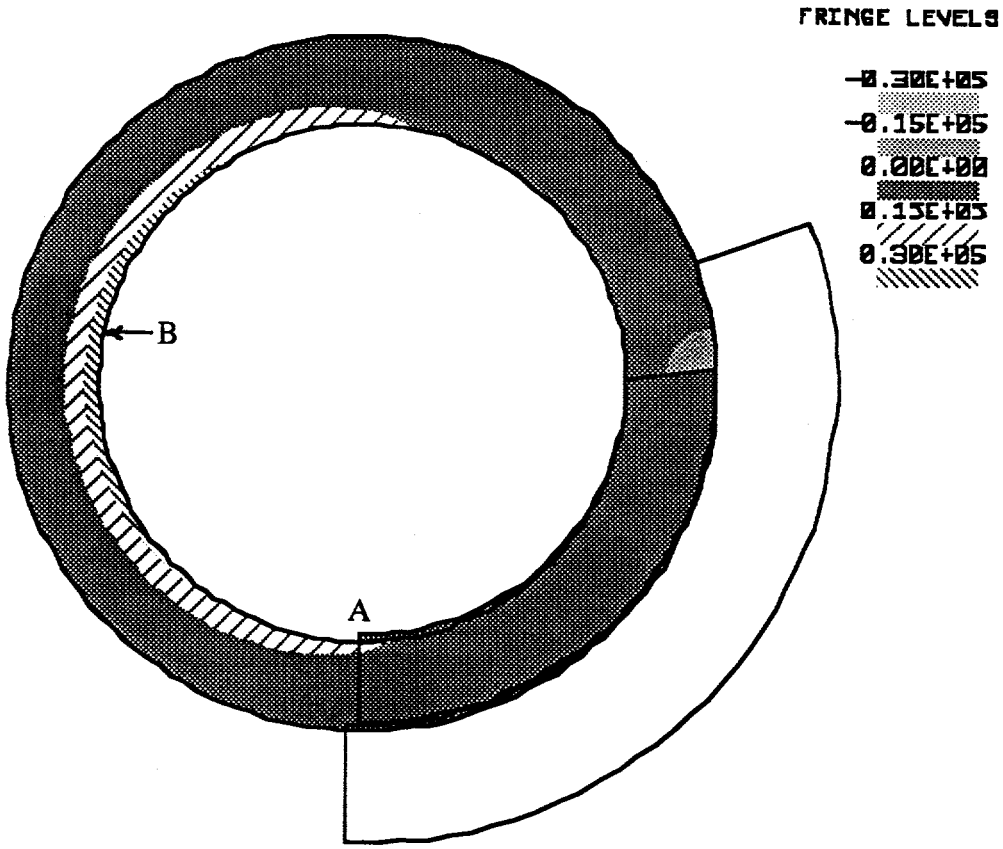

Fig. 4.43 Final chip geometry and maximum principal stress fringes for C-48 groove for feed of 0.0091 in/rev and cutting speed of 40 in/s .

The required displacement of the chip to reach the yield strength of 30,000 psi can be expressed in terms of the change in circumference of the chip relative to its original circumference. The maximum principal stress as a function of the change in chip circumference is shown in Figs. 4.44 and 4.45 for the C-68 and C-48 inserts, respectively, for a cutting speed of 40 in/sec. As the feed is increased, a smaller change in the circumference is required to cause breaking. This is in agreement with the cutting tests that showed that the chips broke more readily for the higher feeds.

Note that for chips to break, the free end of the chip must remain in contact with the flank face of the tool. The chip contact force arises from the friction between the chip and the tool, and the stiffness of the chip. It was shown in Section 3 that the stiffness of the chip is inversely proportional to the third power of the radius of curvature. Therefore, a chip with a small curvature is more likely to remain in contact with the tool flank face because a large out-of-plane force would be required to cause it to slip. This can be seen in Fig. 4.46, which shows the force as a function of the out-of-plane displacement for the C-68 tool. For a given displacement, the force required to cause the chip to slip out-of-plane increases as the feed is increased. Therefore, for small feeds only a small force would be required to cause the chip to slip, making it unlikely that it would remain in contact with the tool and break.

Figure 4.47 shows similar results for the C-48 insert. Note that for the same out-of-plane displacement and feed, a larger force would be required to cause the chip to slip so that a smaller land insert is more likely to break chips.

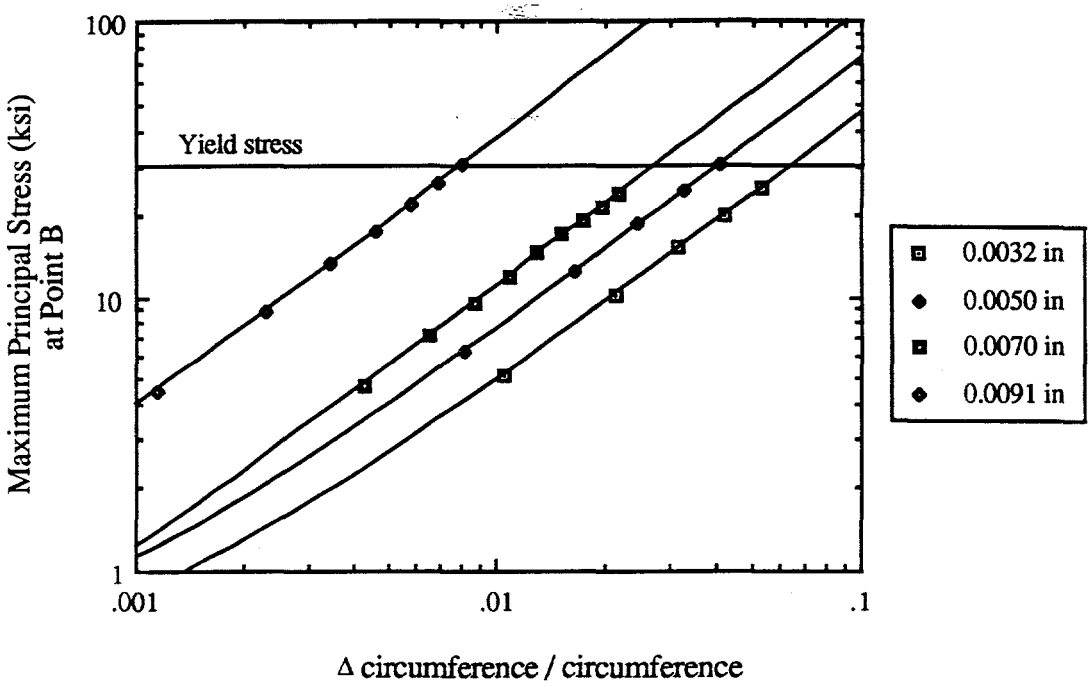

Fig. 4.44 Maximum principal stress versus change in circumference for C-68 insert for the cutting speed of 40 in/s.

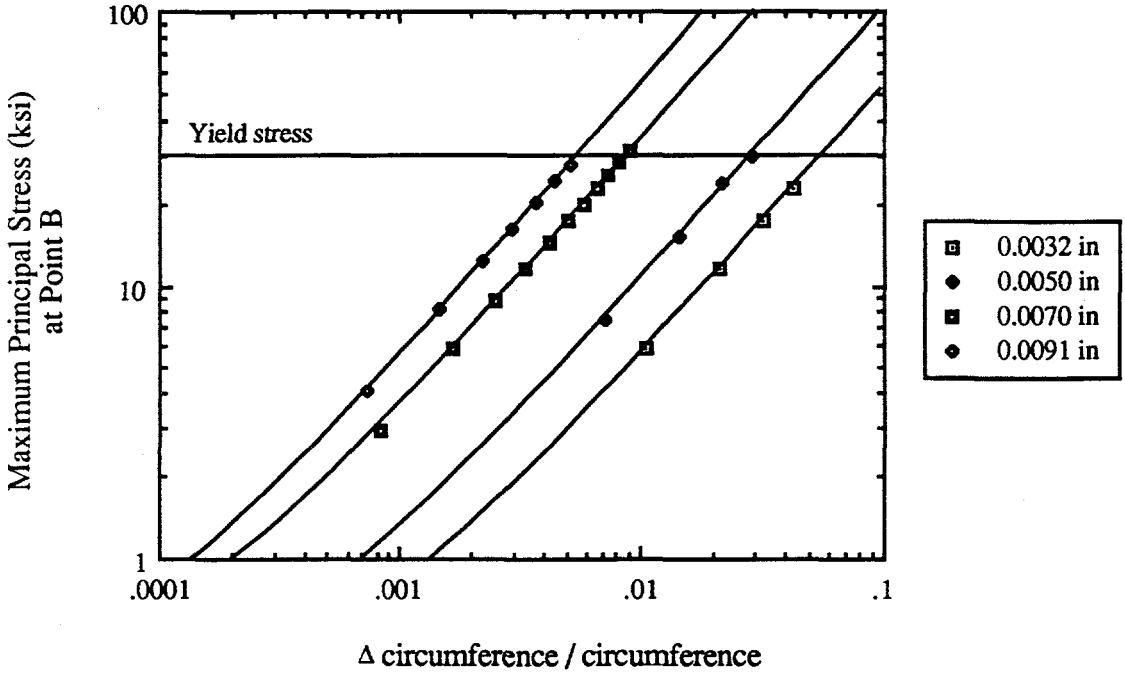

Fig. 4.45 Maximum principal stress versus change in circumference for C-48 insert for the cutting speed of 40 in/s.

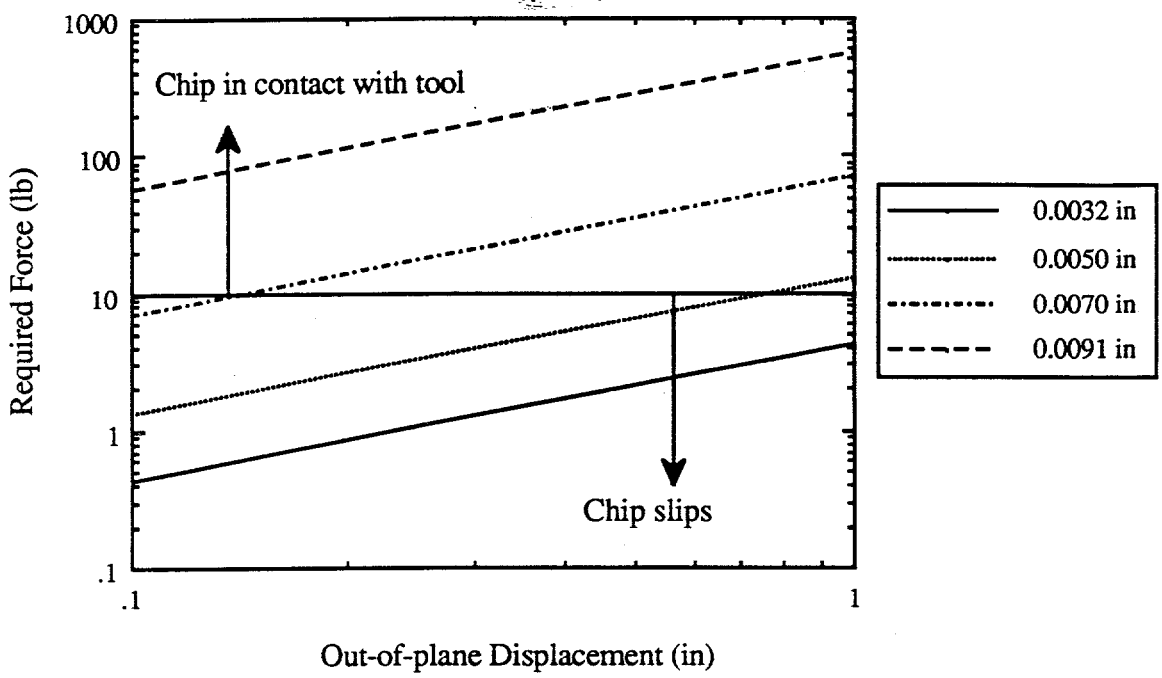

Fig. 4.46 Chip out-of-plane displacement for C-68 insert

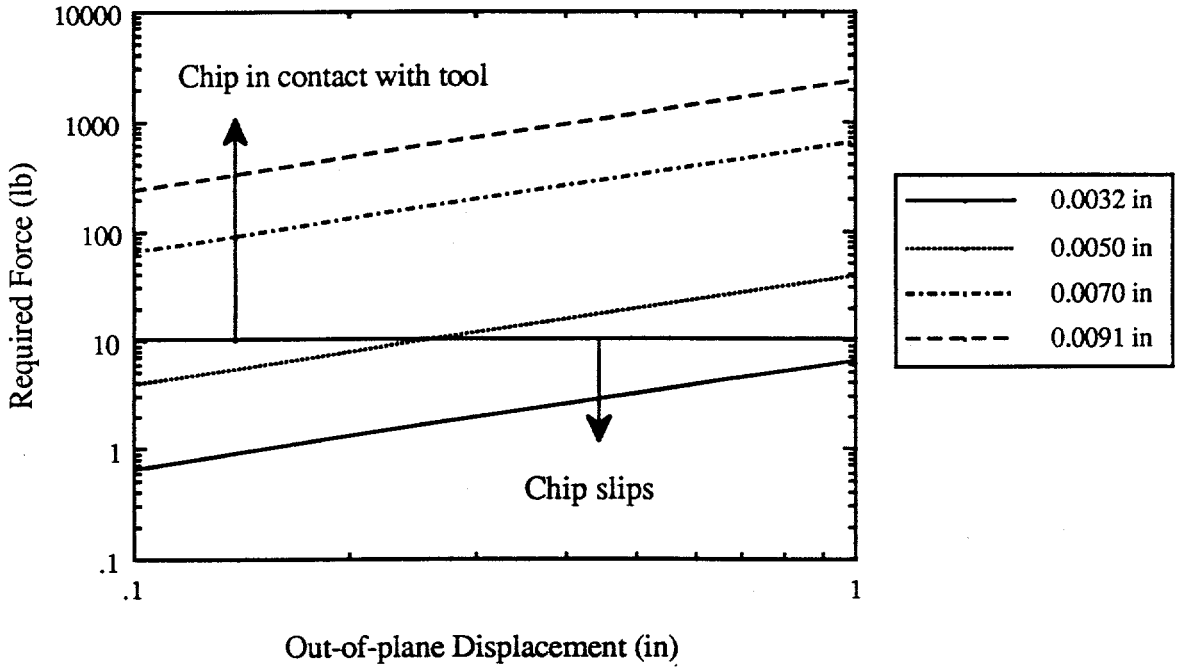

Fig. 4.47 Chip out-of-plane displacement for C-48 insert

5. Summary and Conclusions

This project has demonstrated the feasibility of using a finite element model of the cutting process to determine the chip breakability of groove-type inserts under various cutting conditions. As part of the project, the existing viscoplastic model of orthogonal cutting was modified to simulate steady state cutting using a groove-type chip breaker tool. The model can be used to predict chip thickness, chip radius, total strain, the cutting force components, and the temperature distribution in the chip and the tool.

Deformation of the chip beyond its initial geometry was determined with a second model that simulated the chip after formation. The chip was modeled with an updated-Lagrangian large deformation code called NIKE2D. Using the initial chip geometry derived from the orthogonal cutting model, a plane strain model of the entire chip was developed that included the support reactions of the chip along the flank face of the tool. Thus, the two models were used together to determine the likelihood of chip breaking for a particular insert geometry.

The models were verified with cutting tests which included three different grooved inserts and a comparable grade flat insert. The workpiece material was 1020 steel. Cutting tests were conducted for four feeds and three cutting speeds. The measured chip thicknesses, cutting forces, and thrust forces closely matched the predicted values. In general, it was found that the cutting and thrust force components decreased as the land length of the grooved inserts decreased. In addition, the chip thickness and temperature of the chip and tool decreased, while the radius of curvature of the chip increased as the land length decreased.

It was found in this study that the ratio of the chip thickness to its radius plays a significant role in chip breaking. Strain produced in the circular chip because of deformation is directly proportional to this ratio. Therefore, chip breakability is improved for thick chips with a small radius, which results in a large thickness to radius ratio. In addition, a precondition for chip breaking is that the free end of the chip must remain in contact with the tool flank face. The stiffness of the chip is inversely proportional to the cube of the chip radius. Therefore, it is more likely that a smaller radius chip will remain in contact with the tool, and it will be more likely to break. Note that this requirement is also consistent with a large chip thickness to radius ratio for good chip breakability.

A wide range of chip forms was obtained for the tested speeds and feeds. The prediction of chip failure from the model was in agreement with the experimental observations. The chip broke about halfway along the circumference, where the highest maximum principal stress was present. Also, the support reactions at the free end of the chip required to sustain the stress level at failure were found to be reasonable. The required out-of-plane force causing the chips to slip was small for lower feeds, which made

it harder to break the chips at lower feeds. This was in agreement with the experimental observations.

Based on the experimental observations, a critical thickness to radius ratio was found for which chips would break. The critical ratio was significantly effected by the cutting speed. However for the smallest feeds, the thickness to radius ratio was invariant with speed for all the inserts investigated. This result is important because it indicates that the difficulty in breaking chips at higher speeds is due to the increased mechanical strength of the chip, rather than a reduction in stress in the chip. A possible explanation for this is that the temperature of the chip increases at higher speeds, thus making it more ductile and less likely to break.

5.1 Future Work

Future work should be directed towards exploring the applicability of the results of this project to other feeds, speeds, workpiece materials, and cutting tools. In particular, chip breaking at lower feeds and higher speeds should be studied.

This research project focused on groove-type inserts. Future work should investigate other types of chip breakers, such as obstruction-type breakers. As described in this report, thick and tightly-curled chips are more likely to break. Future work should concentrate on optimizing cutting tool geometries and establishing cutting conditions for which chips could be broken reliably.

In this study, the orthogonal cutting model was modified to simulate groove-type chip breakers. Simulation of other types of chip breakers, including custom-designed tools, will require further modification of the cutting model. In addition, the dependence of the mechanical strength of the chip on the cutting speed emphasizes the need to predict mechanical strength as a function of the cutting conditions and the tool geometry. The strength is a function of the cutting temperature, the strain, and the strain-rate in the chip. These can be predicted with the cutting model. By relating these parameters to the mechanical strength of the chip, it would be possible to ultimately determine if a chip is likely to break.

6. References

1. Perzyna P., " Fundamental Problems in Viscoplasticity ", *Recent Advances in Applied Mechanics*, Ch. 7, 1969.

2. Zienkiewicz O. C. and Godbole P. N., " Flow of Plastic and Visco-Plastic Solids With Special Reference to Extrusion and Forming Process", *Int. Jour. of Mech. Sci.*, vol. 8, 1974, p. 3.

3. Peter B., " Infinite elements ", *Int. Jour. of Mech. Sci.*, vol. 11, 1977, p. 53-64.

4. Zienkiewicz O. C., " Flow of Solids During Forming and Extrusion : Some Aspects of Numerical Solutions ", *Int. Jour. of Solids and Structure*, vol. 14, 1978, p 15.

5. Sani, " The Cause and Cure of the Superior Pressure Generated by Certain FEM Solutions of Incompressible Navier-Stokes Equations ", *Int. Jour. of Mech. Sci.*, vol. 1, 1981, p. 17-43.

6. Chao B. T., " Control Contact Cutting Tools ", *Jour. of Eng. for Ind.*, May 1959, p. 139-151.